Available online at www.sciencedirect.com
SCIENCE DIRECT®
Chemical Engineering and Processing 42 (2003) 621–643
Chemical Engineering and Processing
www.elsevier.com/locate/cep

Prediction of the gas–liquid volumetric mass transfer coefficients in surface-aeration and gas-inducing reactors using neural networks

R. Lemoine [a], B. Fillion [a], A. Behkish [a], A.E. Smith [b], B.I. Morsi [a,*]

[a] Chemical and Petroleum Engineering Department, University of Pittsburgh, 1249 Benedum Hall, Pittsburgh, PA 15261, USA
[b] Industrial and Systems Engineering Department, Auburn University, Auburn, AL, USA

Received 6 May 2002; received in revised form 30 October 2002; accepted 30 October 2002

Abstract

Almost all available literature correlations to predict the volumetric gas–liquid mass transfer coefficient, k_La in agitated reactors are systems- or operating conditions-dependent. In this study, two back-propagation neural networks (BPNNs), one dimensional and one dimensionless were developed to correlate k_La for numerous gas–liquid systems in both surface-aeration reactors (SAR) and gas-inducing reactors (GIR) operating under wide ranges of industrial conditions. A total of 4435 experimental data points obtained from more than 10 publications for 50 gas–liquid systems were used to train, validate the dimensional and dimensionless BPNNs, which were able to correlate all k_La values with R^2 of 90.5 and 88.6%, respectively. The dimensional BPNN was used to predict the effect of various operating parameters on k_La in a number of important industrial processes. The predictions showed that increasing liquid viscosity decreased k_La values in the SAR, while k_La values in the GIR increased and then decreased with increasing liquid viscosity, following the gas holdup behavior. Increasing liquid density decreased k_La in both reactor types. Increasing liquid surface tension increased k_La values in the SAR, whereas in the GIR, k_La decreased due to the increase of bubble size. Increasing gas diffusivity or gas partial pressure or mixing speed, increased k_La in both reactor types. k_La values in the GIR were always higher than those in the SAR and increasing $D_{Imp.}/D_T$ and H_F/H_L increased k_La in both reactor types.

Keywords: Back-propagation neural network; Gas–liquid systems; Gas-inducing reactors; Surface-aeration reactors; Volumetric gas-liquid mass transfer coefficient

1. Introduction

The design, scale-up and optimization of industrial processes conducted in multiphase agitated reactors require, among others, precise knowledge of the hydrodynamics, mass and heat transfer parameters and reaction kinetics. Literature data available indicate that the gas–liquid mass transfer is generally the rate-limiting step in many industrial processes [1] and hence the focus of this paper is on the assessment of the volumetric gas–liquid mass transfer coefficient, k_La, in agitated reactors. Tables 1 and 2 present available literature correlations for k_La in surface-aeration reactors (SAR) and gas-inducing reactors (GIR), respectively. From these tables it appears that these correlations were proposed to predict k_La values for a specific gas–liquid system under ambient conditions or high pressures and temperatures as a function of dimensionless numbers [3–6,8,15–23], specific power input [2,3,7,11–13,24] or non-linear statistical correlations [9,10]. Although supposedly independent of the gas–liquid system, k_La values predicted using the dimensionless correlations often provide large deviations when compared with experimental data [25–27]. Similarly, k_La predicted using the specific power input correlations frequently deviates from the actual experimental values obtained under typical industrial conditions, since these correlations do not directly account for the effects of pressure and/or temperature on k_La. The statistical correlations, on the other hand, are claimed to predict k_La with confidence levels greater than 97.5% [9,10,28,29], but they are specific to the gas–liquid system and reactor employed. Thus, there is a great need for developing k_La correla-

* Corresponding author. Fax: +1-412-624-9639.
E-mail address: morsi@engrng.pitt.edu (B.I. Morsi).

0255-2701/03/$ - see front matter
doi:10.1016/S0255-2701(02)00211-8

Table 1
Literature survey on k_La in SAR

Author	Gas	Liquid	Operating conditions	Correlations
Matsumura et al. [2]	–	Water, alcohols	–	$k_La/\sqrt{D_O} = 309(P^*/V_L)^{0.6}\varepsilon_G^{0.6}$
Albal et al. [3]	O_2	Water	13.8–96.5 bar 298 K 13.3–20 Hz	$k_La = 2.579 \times 10^{-2} D_A^{0.5}(P^*/V_L)^{0.6}\varepsilon_G^{0.6}$
Albal et al. [3]	O_2	Water, glycerin, CMC, triton CF-32	6–97 bar 295–573 K	$Sh = 1.41 \times 10^{-2} Sc^{0.5} Re^{0.67} We^{1.29}$
Versteeg et al. [4]	CO_2 N_2O	Water, alkanol–amine aqueous	1.3–10.1 bar 291–356 K $179 < Re < 12471$ $117 < Sc < 13487$	$Sh = 0.064 Sc^{0.5} Re^{0.72}$
Mizan [5]	H_2 C_2H_4 C_3H_6	C_3H_6 *n*-hexane	$0.922 < Fr < 2.073$ $67100 < Re < 1643000$ $0 < Ws < 30$	$Sh = 51.7 \times 10^9 Fr^{2.20} Re^{-1.12}(1-Ws)^{4.31}$
Mizan et al. [6]	H_2 C_2H_4	C_3H_6	$0.922 < Fr < 2.073$ $198000 < Re < 445100$ $741 < We < 31060$	$Sh = 55.2 Fr^{2.07} Re^{1.20} We^{-1.34}$
Wu [7]	Air	Water+Na_2SO_3+$CoSO_4$	$1.2 < P^*/V_L < 8.5$ kW/m^3	$k_La = 6.34 \times 10^{-2}(P^*/V_L)^{0.65}$
Tekie et al. [8]	N_2 O_2	Cyclohexane	$2100 < We < 13300$ $1 < Fr < 3$	$Sh = 4.51 \times 10^3 We^{-0.21} Fr^{0.92}$
Tekie et al. [9]	N_2 O_2	Cyclohexane	x_1: $6.67 < N < 20.00$ Hz x_2: $7 < P < 35$ bar x_3: $330 < T < 430$ K x_4: $0.171 < H < 0.268$ m	N_2: $\ln(k_La) = -2.90 + 0.358x_1 + 0.071x_2 + 0.285x_3 - 0.184x_4 - 0.393x_1^2 - 0.059x_2^2 + 0.044x_3^2 + 0.063x_4^2 - 2.902 \exp(-0.2(x_1 - 0.204)^2) + 0.044 \exp(0.1(x_1+3)(4-x_4))$ O_2: $\ln(k_La) = -2.933 + 0.106x_1 + 0.096x_2 + 0.231x_3 - 0.122x_4 - 0.382x_1^2 - 0.05x_2^2 - 0.031x_3^2 + 0.07x_4^2 - 2.902 \exp(-0.173(x_1)^2) + 0.114 \exp(0.1(x_1+3)(4-x_4))$
Fillion and Morsi [10]	N_2 H_2	Soybean oil	x_1: $373 < T < 473$ K x_2: $10 < N < 23.3$ Hz x_3: $0.171 < H < 0.268$ m x_4: $1 < P < 5$ bar	N_2: $\ln(k_La) = -6.50 + 0.177x_1 + 0.474x_2 - 0.407x_3 + 0.053x_3^2 - 0.0798x_2x_3$ H_2: $\ln(k_La) = -5.99 + 0.229x_1 + 0.471x_2 - 0.473x_3 - 0.0445x_1^2 + 0.0524x_3^2 - 0.126x_2x_3$

tions in agitated reactors, which would be system-independent and could be used for proper design and scale-up of industrial processes.

Recently, artificial neural networks (ANNs) have been employed in different industrial applications in order to describe, control or model complex chemical processes, as shown in Tables 3 and 4. Iliuta et al. [35] used neural networks to correlate a and k_La in trickle-bed reactors over wide ranges of industrial operating conditions. Yang et al. [25] developed a neural network to correlate k_La in gas sparging reactors (GSR), operating under atmospheric conditions, however, their study was limited to oxygen transfer into a Newtonian coalescing liquid.

The purpose of this study is to develop a more general and system-independent correlation based on back-propagation neural networks (BPNN), which accounts for the various observed trends of k_La in the literature for SAR and GIR. The methodology used to develop and validate the neural networks was described and one dimensionless and another dimensional ANN correlations were developed. The dimensional neural network

Table 2
Literature survey on k_La in GIR

Authors	Induction type	Gas	Liquid	Operating conditions	Correlations
Joshi and Sharma [11]	Hollow shaft+Hollow impeller	CO_2	Na_2CO_3+$NaHCO_3$	$0.41 < D_T < 1.0$ $0.35 < D_{Imp.}/D_T < 0.75$ $H_B/D_T < 0.5$ $D_{Imp.}/10 < H_{Imp.} < D_{Imp.}/3$ $3 < N < 11.7$ Hz $0.0003 < U_G < 0.032$ m·s^{-1} $1 < P^*/V_L < 15$ kW/m^3 $0.04 < k_La < 0.3$ s^{-1}	$U_G < 0.005$: $k_La = 6.8 \times 10^{-3}(P^*/V_L)^{0.55}U_G^{0.5}$ $U_G > 0.005$: $k_La = 3.26 \times 10^{-3}(P^*/V_L)^{0.55}U_G^{0.25}$
Kara [12]	Hollow shaft+Rushton turbine	H_2	Tetraline SRCII	70−135 bar 606−684 K 50−400 rpm $P^*/V_L < 119$ W/m^3	$k_La = (3.43 \pm 1.13) \times 10^{-4}(P^*/V_L)^{0.80 \pm 0.09}(H_L/D_T)^{-1.9 \pm 0.66}$
Sawant et al. [13]	Denver type impeller	Air	Water+sodium sulfate	$5 < N < 36$ rev/s $0.5 < H'/D_{Imp.} < 1.5$	$k_La = 0.0195 \times (P^*/V_L)^{0.5}$
Karandikar et al. [14]	Hollow shaft+Rushton turbine	CO H_2 CO_2 CH_4	F-T wax F-T wax+water	7−45 bar 423−498 K 700−1000 rpm	*CO and H_2:* $k_La = 0.1607(N/1000)^{3.42}$ exp(0.108 × P)−0.046 *CO_2 and CH_4:* $k_La = 0.0171(N/1000)^{6.05}$ exp(0.38 × P)+0.00525
Chang et al. [15]	Hollow shaft+Rushton turbine	N_2 H_2 CH_4	*n*-hexane	$177 < Eu < 2232$ $1913 < We < 7239$ $8.6 < Sc < 28.5$ $146\,000 < Re < 290\,000$	$Sh = 6.67 \times 10^{26}Re^{-2.6}Sc^{0.1}Eu^{-1.0}We^{4.2}$
Chang and Morsi [16]	Hollow shaft+Rushton turbine	N_2 CH_4	Water, *n*-hexane	$560 < Eu < 10\,960$ $760 < We < 7410$ $14 < Sc < 128$ $102\,400 < Re < 282\,600$	$Sh = 2.39 \times 10^{-28}Re^{4.86}Sc^{2.55}Eu^{0.350}We^{0.34}$
Chang and Morsi [17]	Hollow shaft+Rushton turbine	N_2 H_2 CH_4	*n*-decane	$1582 < We < 6528$ $63\,433 < Re < 216\,626$ $1.15 < Fr < 2.59$	$Sh = 2.95 \times 10^{14}Re^{-1.41}Fr^{4.74}We^{-1.32}$
Dietrich et al. [18]	Hollow shaft+Rushton turbine	H_2	Water, ethanol, hydrogenation mixt. of adiponitril	$V_R = 500$ ml $0.25 < V_L < 0.38$ dm^3	$H/D_T = 1$: $Sh = 3 \times 10^{-4}Re^{1.45}Sc^{0.5}We^{0.5}$ $H/D_T = 1.4$: $Sh = 1.5 \times 10^{-4}Re^{1.45}Sc^{0.5}We^{0.5}$
Hichri et al. [19]	Hollow shaft+Turbine	H_2	2-propanol *o*-cresol	$10^4 < Sh < 5 \times 10^5$ $7 \times 10^3 < Re < 13 \times 10^4$ $500 < Sc < 900$ $180 < We < 550$ $1.2 < V_G/V_L < 1.7$	$Sh = 0.123Re^{0.44}Sc^{0.5}We^{1.27}(V_G/V_L)^{1.1}$
Chang and Morsi [20]	Hollow shaft+Rushton turbine	CO	*n*-hexane *n*-decane *n*-tetradecane	$730 < Eu < 10\,737$ $8 < Sc < 487$ $1688 < We < 11\,332$ $39\,506 < Re < 333\,924$	$Sh = 3.41 \times 10^{-20}Re^{3.06}Sc^{2.43}Eu^{0.16}We^{0.93}$

Table 2 (*Continued*)

Authors	Induction type	Gas	Liquid	Operating conditions	Correlations
Chang [21]	Hollow shaft+Rushton turbine	CO CO_2 CH_4	*n*-C6 *n*-C10 *n*-C14	$546 < Eu < 11\,320$ $8 < Sc < 491$ $31\,101 < Re < 338\,409$ $1.2 < Fr < 2.6$	$Sh = 5.114 \times 10^{-12} Re^{2.18} Sc^{1.63} Eu^{0.28} Fr^{1.73}$
Chang [21]	Hollow shaft+Rushton turbine	H_2	*n*-C6 *n*-C10 *n*-C14	$569 < Eu < 10\,468$ $1676 < We < 7721$ $10 < Sc < 151$ $68\,926 < Re < 264\,882$	$Sh = 2.74 \times 10^{-18} Re^{3.00} Sc^{2.21} Eu^{-0.42} We^{1.29}$
Koneripalli et al. [22]	Hollow shaft+Rushton turbine	N_2 CO H_2 CO_2 CH_4	Methanol, ethanol	$288 < Eu < 9640$ $7 < Sc < 220$ $63\,000 < Re < 385\,000$ $2000 < We < 14\,700$	$Sh = 4.88 \times 10^{6} Re^{-3.81} Sc^{0.23} We^{4.48} Eu^{0.09}$
Heim et al. [23]	Hollow shaft	Air	Water, fermentation mixtures	$0.28 < Fr^* < 1.49$ $33\,000 < Re < 260\,000$	*4-pipe impeller:* $Sh^*/9.5 \times 10^{-5} = 1 - \exp(-19.64 Re^{-0.216} Fr^{*1.336})$ *6-pipe impeller:* $Sh^*/1.06 \times 10^{-4} = 1 - \exp(-21.63 Re^{-0.234} Fr^{*1.207})$ *Disk impeller:* $Sh^*/1.04 \times 10^{-4} = 1 - \exp(-1331.20 Re^{-0.557} Fr^{*2.498})$
Tekie et al. [8]	Hollow shaft+Rushton turbine	N_2 O_2	Cyclohexane	$2100 < We < 13\,300$ $1 < Fr < 3$	$Sh = 4.51 \times 10^{3} We^{-0.21} Fr^{0.92} (1 + 1.867 \times 10^{3} \varepsilon_G)$
Tekie et al. [9]	Hollow shaft+Rushton turbine	N_2 O_2	Cyclohexane	x_1: $6.67 < N < 20.0$ Hz x_2: $7 < P < 35$ bar x_3: $330 < T < 430$ K x_4: $0.171 < H < 0.268$ m	N_2: $\ln(k_L a) = 0.009 - 1.922x_1 + 0.102x_2 + 0.269x_3 - 0.050x_4 + 0.723x_1^2 - 0.098x_2^2 + 0.018x_3^2 + 0.014x_4^2 - 3.395 \exp(0.035(x_1 - 4.248)^2) + 0.265 \exp(0.1(x_1 + 3)(4 - x_4))$ O_2: $\ln(k_L a) = -3.707 + 1.235x_1 + 0.105x_2 + 0.216x_3 - 0.087x_4 + 0.092x_1^2 - 0.044x_2^2 + 0.005x_3^2 + 0.056x_4^2 - 3.753 \exp(-0.170(x_1 - 1.604)^2) + 0.209 \exp(0.1(x_1 + 3)(4 - x_4))$
Forrester et al. [24]	Hollow shaft+6 concave blades	Air	Water	$250 < P^*/V_L < 2250$ w/m^3 $0.01 < k_L a < 0.035$ s^{-1}	$k_L a = (76 \pm 21) \times 10^{6} (P^*/V_L)^{0.80 \pm 0.06}$
Fillion and Morsi [10]	Hollow shaft+Rushton turbine	N_2 H_2	Soybean oil	x_1: $373 < T < 473$ K x_2: $10 < N < 23.3$ Hz x_3: $0.171 < H < 0.268$ m x_4: $1 < P < 5$ bar	N_2: $\ln(k_L a) = -4.86 - 0.179x_1 + 0.708x_2 - 0.596x_3 + 0.0759x_1^2 + 0.116x_2^2 - 0.228x_1x_2 - 0.0763x_2x_3 - 0.0754x_1^3 + 0.00269(x_2 + 2.5)e^{2x_3} + 1.28 \tanh(0.3x_2(5.5 - x_3^2)) + 0.1(2 - 4x_3)) - 0.339x_1x_2x_3$ H_2: $\ln(k_L a) = -3.868 + 0.516x_2 - 0.790x_3 + 0.223x_1^2 - 0.352e^{x_1} + 0.326e^{x_3} - 0.00378(x_2 + 3)e^{2.5x_3} + 2.099 \tanh(0.3x_2(8 - x_3^2)) + 0.1(2 - 6x_3)) - 0.927x_1e^{-\lvert x_2 \rvert}$

Table 3
Selected literature survey on ANN in the chemical industry

Authors	Systems used	Model
Alvarez et al. [30]	Newtonian and non-Newtonian fluid in bubble columns	Prediction of k_La
Azlan Hussain [31]	Review	Simulation and online implementation
Fullana et al. [32]	Supercritical fluid extractors	Kinetic modeling
García-Ochoa and Gómez Castro [27]	O_2/H_2O xanthan gum solution in STR	Prediction of k_La
Henrique et al. [33]	pH neutralization process	Model prediction and simulation
I et al. [34]	Sugar, cell mass, L-lysine	Modeling
Iliuta et al. [35]	Several system in trickle bed reactors	Prediction of mass transfer coefficient
Jambunathan et al. [36]	Liquid crystal thermography	Evaluation of heat transfer coefficient
Krothapally and Palanki [37]	Batch process	Process optimization
Larachi et al. [38]	3-phase fluidized bed reactor	Prediction of U_{Lmf}
Leib et al. [39]	Fluidized bed	Simulation of propylene oxidation
Leib et al. [40]	3-phase bubble column	Simulation of Fischer-Tropsch process
Mills et al. [41]	Conical tank, industrial evaporator	Control
Nascimento and Giudici [42]	Nylon-6,6 polymerization	Process optimization
Nascimento et al. [43]	Chemical process	Optimization
Nikravesh et al. [44]	CSTR	Control of h and E_0
Qi et al. [45]	Fixed-bed reactor	Prediction of overall heat transfer coefficient
Reisener et al. [26]	Electrolyte solutions gas sparged reactors	Prediction of k
Sharma et al. [46]	$H_2/CO–SiO_2–Al_2O_3$ fixed bed reactor	Modeling of Fischer-Tropsch process
Shaw et al. [47]	–	Nonlinear process modeling
Tendulkar et al. [48]	Fixed-bed reactor	Predictive control of flow rate and temperature
Thibault and Grandjean [49]	–	Prediction of Nu number
Wilson and Zorzetto [50]	Hybrid process	Control
Yang et al. [25]	Various system in STR	Prediction of k_La
Zhou et al. [51]	Fixed bed reactor	Modeling

correlation was employed to predict k_La behavior in different important industrial processes.

2. Neural networks

Traditionally, ANNs have been used to model complex non-linear systems [25,31,32,35,38,40,49] and appeared to be a good alternative to traditional empirical, phenomenological or statistical correlations [25,26,35,38]. The ANNs are more powerful and can manipulate non-linear input–output relationships more successfully than available literature conventional correlations [52].

2.1. Systems studied

A significant number of experimental data (4435 points) were used to develop k_La neural network correlations. These data were obtained for different gas–liquid systems and cover wide ranges of operating conditions, reactor types (SAR and GIR) and geometries as well as liquid and gas natures, as can be seen in Table 5. The operating conditions used were similar to those employed in industrial processes including, cyclohexane oxidation [8,55], soybean oil hydrogenation [10,57], propylene polymerization [28,54] and Fischer–Tropsch synthesis [14,58]. These data indicate that k_La values are affected by several variables, which are grouped as follows [59]:

- Geometrical variables: reactor diameter (D_T), impeller diameter ($D_{Imp.}$), and impeller height from the bottom of the reactor (H_F).
- Operating variables: reactor mode (SAR, GIR), mixing speed (N), liquid height (H_L), liquid height above the impeller (H), temperature (T), and gas partial pressure (P_l).
- Physicochemical variables: liquid viscosity (μ_L), liquid and gas densities (ρ_L and ρ_G), liquid surface tension (σ_L) and the gas diffusivity in the liquid (D_L).

A dimensional analysis [60] was performed using these variables and 9 dimensionless groups were obtained: Re, Fr, Sc, We, Eu, ρ_G/ρ_L, $D_{Imp.}/D_T$, $D_{Imp.}/H_F$ and $D_{Imp.}/H_L$.

2.2. BPNNs

Two BPNNs, one dimensional and one dimensionless, each with its own input were constructed. The inputs to the dimensional BPNN were the geometrical, operating and physicochemical variables as shown in Table 6a, whereas the inputs to the dimensionless BPNN were the dimensionless groups as presented in Table 6b. An additional input, the 'reactor operating mode', was added in both BPNNs as shown in these tables.

2.2.1. Model and architecture

The critical step in building a robust ANN is to create an architecture, which should be as simple as possible and has a fast capacity for learning the data set. The robustness of the ANN will be the result of the complex interactions between its topology and the learning

Table 4
Application of ANNs in multi-phase reactors

Authors	System studied IU	Reactor type	Output parameters	ANN type and topology
Alvarez et al. [30]	CO_2/Sucrose and CMC	Bubble column	k_La	BPN-FF
García-Ochoa and Gómez Castro [27]	O_2/H_2O xanthan gum sol.	Baffled stirred tank	k_La	FF-ML 13-4-1
Iliuta et al. [35]	$805 \leqslant \rho_L \leqslant 1450$ $6.32 \times 10^{-4} \leqslant \mu_L \leqslant 4.72 \times 10^{-2}$ $1.06 \times 10^{-2} \leqslant \sigma_L \leqslant 7.77 \times 10^{-2}$ $0.937 \leqslant \rho_G \leqslant 57.46$ $5.4 \times 10^{-4} \leqslant d_P \leqslant 2.64 \times 10^{-2}$	Trickle beds	Sh_G, Sh and $a.d_V/(1-\varepsilon)$	FF-ML 7-13-1, 7-8-1, 8-11-1
Larachi et al. [38]	$780 \leqslant \rho_L \leqslant 1623$ $8.9 \times 10^{-4} \leqslant \mu_L \leqslant 0.0719$ $0.025 \leqslant \sigma_L \leqslant 0.073$ $1.145 \leqslant \rho_G \leqslant 1.159$ $1290 \leqslant \rho_S \leqslant 7510$	3-Phase fluidized beds	U_{Lmf}, Re_L	FF-ML 8-6-1, 5-9-1
Leib et al. [39]	Propylene oxidation process	Fluidized bed	u_{sb}, y_i, y_{4-6}, w_i, w_{4-6}	FF-ML 11-8-9
Leib et al. [40]	Liquid-phase Fischer-Tropsch system	Slurry bubble column	C_G, C_L, U_G	FF-ML 6-5-3
Nikravesh et al. [44]	Non-isothermal system	CSTR	h and E_0	DNNC-FF
Qi et al. [45]	O_2/Benzene/V_2O_5	Fixed-bed	Heat transfer coefficient	FF-ML, 3 ILN and 1 OLN
Reisener et al. [26]	Electrolyte solution	Gas sparged	k	FF-ML 3-4-1, 3-10-1
Sharma et al. [46]	$H_2/CO/SiO_2-Al_2O_3$	Fixed bed	% conv., liq. conc., CH4 SS conc., SS conc. oxygenates, SS conc. hydrocarbons	ML, 3 ILN and 1 OLN
Tendulkar, et al. [48]	H_2O_2/phenol/Ti-based zeolite cat.	Fixed bed	Phenol flow rate and T	FF-ML, 4-5-2
Yang et al. [25]	$0 \leqslant P_g/V_L \leqslant 55\,000$ $0.8 \leqslant \mu_L \leqslant 70.2$	Stirred tank	k_La	FF-ML, 6-11-1

scheme. The choice of the input variables is the key to insure complete description of the systems, whereas the quality as well as the number of the training observations (experimental data) have a tremendous impact on both the reliability and performance of the ANN. The two BPNNs used were constructed as follows:

(1) One input layer; one output node; two hidden layers; all neurons were interconnected and all connections were weighted.

(2) Each neuron possessed a bias.

(3) The transfer function was a sigmoid of the form:

$$F(x) = \frac{1}{1 + \exp(-x)} \quad (1)$$

The basic architecture of the BPNNs is given in Fig. 1. The number of neurons, (n) and (m) in the first and second hidden layers were determined based on the analysis of errors during the training step of the networks. The PITTNET software developed at the University of Pittsburgh was used to build and validate the two created BPNNs. The matrix formulation for the calculation methodology is briefly described in the Appendix B.

2.2.2. Training or learning phase: back-propagation algorithm

The learning algorithm for the back-propagation, which is commonly accepted [61–63], was used for the development of the ANNs. In this algorithm, the training was supervised by means of a known output data set and the connection weights were adjusted according to the gradient descent method, as the mean squared error (MSE) was minimized towards the smallest error possible [61–63]. More precisely, the training data were fed forward leading to the calculation of the output and associated errors. Then, the associated errors were back-propagated and the adjustment of the weights was completed accordingly [52,61–63]. This process was repeated until the MSE between the experimental and calculated (k_La) values was less than the chosen tolerance (10^{-7}). The mean absolute errors (MAE), the root mean squared errors (RMSE) and the R^2 values were also calculated and used in the validation and construction procedures. Additional details of the back-propagation algorithm are given in Fig. 2. It should be noted that two phenomena were taken into consideration during the construction and validation of the BPNNs. The first phenomenon is over-training, mainly attributed to a large number of iterations, which generally leads to an excellent prediction of the training data set, while predicting poorly the untrained values.

Table 5
Systems studied

Authors	Number of data points	Liquid	Gas	T, K	P_1, bar	Reactor mode	N, rpm	D_T, m	$D_{Imp.}$, m	H_L, m	H_F, m
Chang [21]	272	Water	N_2	328–378	13.7–36.9	GIR	800–1200	0.127	0.0635	0.242–0.250	0.0670
			CO		13.3–36.4						
Chang [21]	274	*n*-hexane	H_2	328–378	5.9–48.4	GIR	800–1200	0.127	0.0635	0.248–0.267	0.0670
			N_2		5.5–50.9						
			CO		6.7–44.5						
			CH_4		5.0–34.3						
Chang [21]	273	*n*-decane	H_2	328–378	9.2–55.8	GIR	800–1200	0.127	0.0635	0.247–0.282	0.0670
			N_2		7.9–51.1						
			CO		7.1–49.7						
			CH_4		7.2–44.9						
Chang [21]	292	*n*-tetrade-cane	H_2	328–378	9.1–59.6	GIR	800–1200	0.127	0.0635	0.245–0.273	0.0670
			N_2		8.4–53.8						
			CO		8.3–52.9						
			CH_4		7.5–48.0						
Chang [21]	291	C_6H_{12}	H_2	328–378	7.5–56.7	GIR	800–1200	0.127	0.0635	0.246–0.281	0.0670
			N_2		7.2–51.8						
			CO		6.7–48.5						
			CH_4		5.3–41.4						
Koneripalli [53]	326	Methanol	N_2	328–428	5.4–49.2	GIR	800–1200	0.127	0.0635	0.245–0.265	0.0670
			CO		4.4–49.4		800–1400				
			H_2		3.3–54.8		800–1400				
			CH_4		4.3–40.9		800–1200				
			CO_2		3.3–23.7		800–1200				
Koneripalli [53]	296	Ethanol	N_2	328–428	6.0–51.3	GIR	800–1200	0.127	0.0635	0.245–0.265	0.0670
			CO		5.9–50.9						
			H_2		5.4–51.4						
			CH_4		5.4–40.9						
			CO_2		3.2–27.6						
Li [54]	295	Propane	H_2	297–333	6.7–37.6	SAR	800–1200	0.125	0.0508	0.198–0.223	0.0670
Li [54]	292	*n*-hexane	H_2	313–353	9.5–58.0	SAR	800–1200	0.125	0.0508	0.202–0.213	0.0670
			C_3H_8	313–353	1.4–6.8		800–1200			0.202–0.213	
			C_2H_4	333	5.0–15.6		1000			0.207	
			C_3H_6	333	2.8–7.9		1000			0.207	
Mizan [5]	303	*n*-hexane	C_3H_6	313–353	1.6–8.5	SAR	800–1200	0.125	0.0508	0.202–0.213	0.0670
			C_2H_4	–	3.3–29.7						

Table 5 (*Continued*)

Authors	Number of data points	Liquid	Gas	T, K	P_1, bar	Reactor mode	N, rpm	D_T, m	$D_{Imp.}$, m	H_L, m	H_F, m
Mizan [5]	234	Propylene	C_2H_4 H_2	297–333 –	2.4–16.2 3.8–31.6	SAR	800–1200	0.125	0.0508	0.198–0.225	0.0670
Tekie [55]	398	C_6H_{12}	N_2 O_2	330–430 –	5.8–34.1 5.5–33.5	SAR and GIR	400–1200	0.115	0.0508	0.171–0.268	0.0635
Mohammad [56]	235	Benzoic acid	O_2 N_2	473 –	0.9–5.0 0.9–5.0	SAR and GIR	1000 –	0.076	0.0317	0.108 –	0.0413
Fillion [57]	654	Soybean oil	H_2 N_2	373–473 –	1.0–5.0 1.0–5.0	SAR and GIR	600–1400	0.115	0.0508	0.171–0.268	0.0635

Table 6a, b
Ranges of the BPNNs input parameters used in this study

	Y_{max} ($\ln k_La_{max}$) –	Y_{min} ($\ln k_La_{min}$) –	ρ_L, kg m^{-3}	ρ_G, kg m^{-3}	$10^{-5}\times\mu$, N s m^{-2}	$10^{-3}\times\sigma_L$, N m^{-1}	$10^{-9}\times D_A$, m s^{-1}	P_1, bar	Reactor mode –	N, rpm	$D_{Imp.}/D_T$ –	H_F/H_L –
Ranges 6*a*	−0.495	−7.729	309.9–1011.1	0.05–0.27	5.0–668.3	1.2–64.5	3.5–153.9	0.86–59.59	0 = SAR 1=GIR	400–1400	0.406–0.500	0.237–0.444
	Y_{max} ($\log Sh_{max}$) –	Y_{min} ($\log Sh_{min}$) –	*Re*	*Sc*	*Eu*	*We*	*Fr*	ρ_G/ρ_L	Reactor mode –	H_F/D_T	$D_T/D_{Imp.}$ –	$H_L/D_{Imp.}$ –
Ranges 6*b*	5.456	2.088	5571–445 836	0.88–1274.1	85–41 876	285–18 949	0.23–3.52	6.4×10^{-5} –0.16	0 = SAR 1 = GIR	1.05–1.49	2–2.46	3.52–6.20

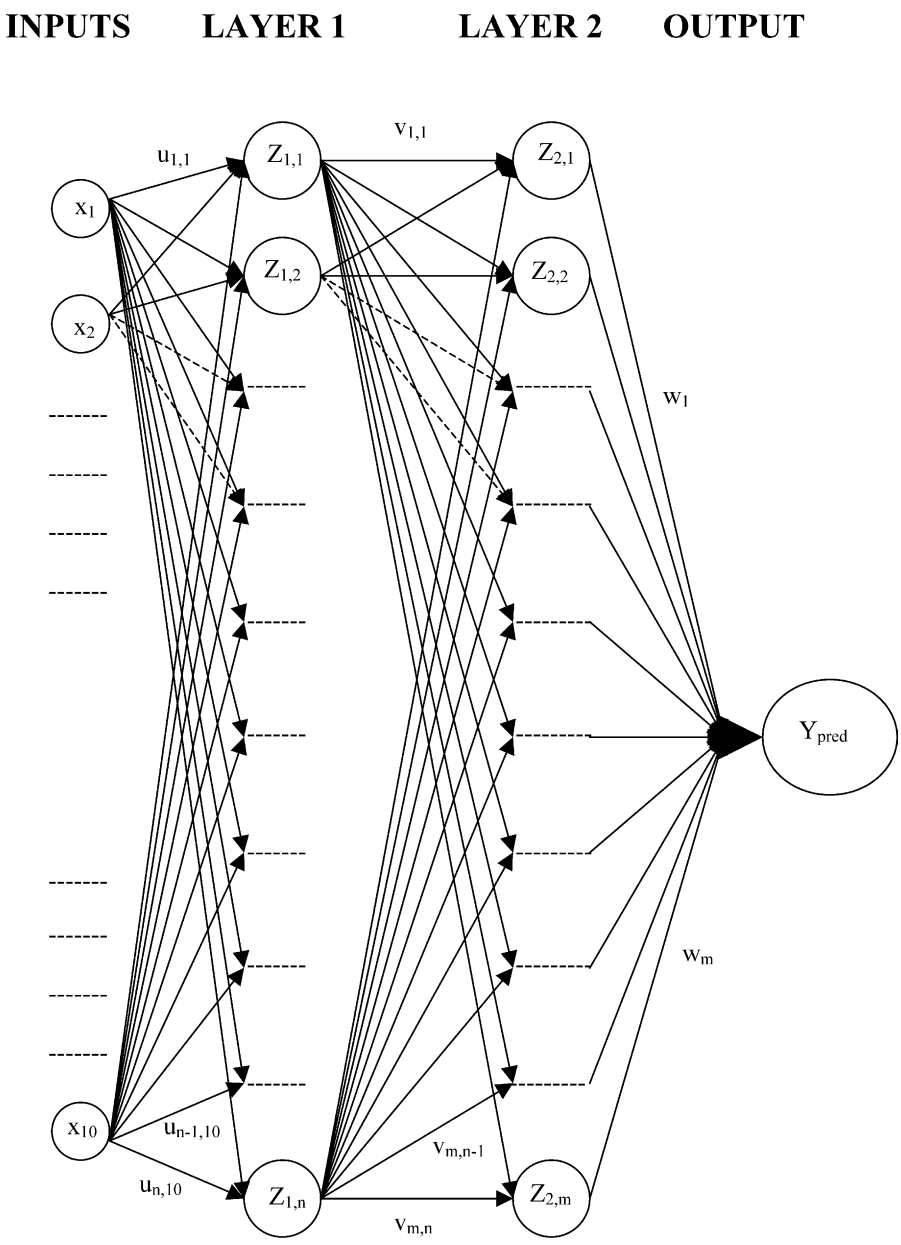

Fig. 1. Architecture of ANN.

The second phenomenon is under-training, which interpolates the untaught values relatively well, while predicting poorly the training data set.

3. Results and discussions

3.1. Architectures choices

All the experimental k_La data points collected were used to build and validate the ANN correlations. In the training algorithm of the BPNNs, the MSE was minimized for each epoch, i.e. iteration. As depicted in Fig. 3, the error appears to decrease with increasing the number of hidden layers and neurons. A minimum error was found for a network topology of 10-23-23-1 and 10-30-30-1 for the dimensional and dimensionless BPNN, respectively. Fig. 3 also shows that the relative error between the networks does not significantly decrease after corresponding topologies of 10-10-1 and 10-15-1. It is important to mention that topologies of 10-23-23-1 and 10-30-30-1 possess a significant number of parameters, 829 and 1291, respectively, representing roughly 1/5 of the data used in the training step. The choice of such topologies could lead to an over-training of the BPNNs and consequently will reduce their ability to accurately interpolate k_La values. On the other hand, the topologies of 10-10-1 and 10-15-1, with only 121 and 181 parameters, appear to be the optimal choice for the construction of the dimensional and dimensionless

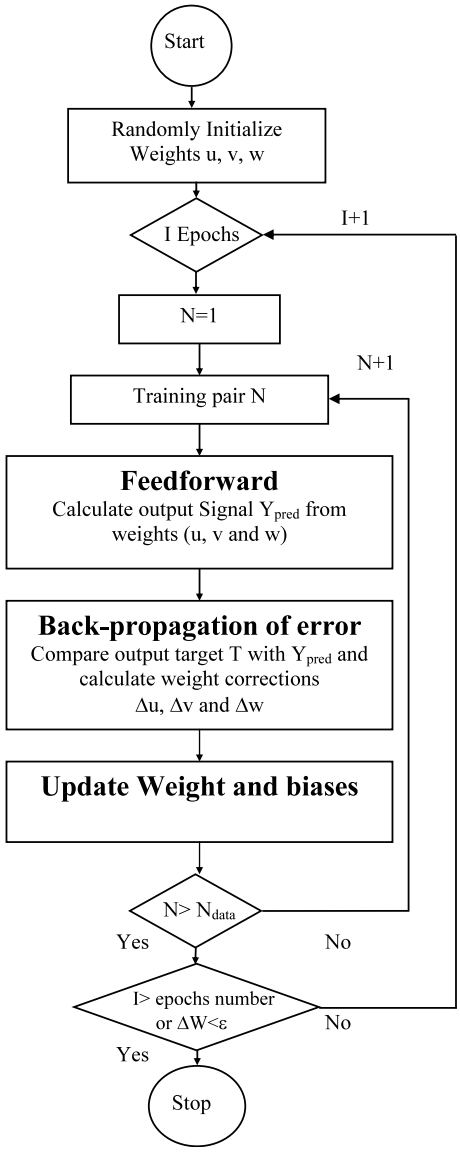

Fig. 2. Back-propagation algorithm.

BPNNs, respectively. It should also be mentioned that a learning rate of 0.25 as suggested in Refs. [52,61–63] was chosen with 10 000 epochs, since as shown in Fig. 4 the MAE and MSE sensibly decrease with the number of iterations. The weights of the two constructed BPNNs are given in Tables 7 and 8.

3.2. Validation of the BPNNs

In the validation step, since the ANN acts as a 'Black Box' and it is almost impossible to determine why a specific BPNN would provide acceptable predictions, two different steps were followed to overcome such a problem. In the first step, cross validation method was used [64,65], where numerous sub-networks with identical architecture and parameters were built and trained using all the experimental data. In the second step, these

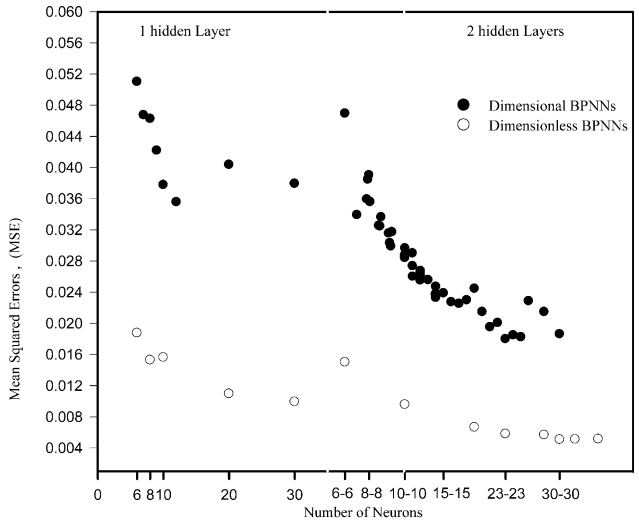

Fig. 3. Error analysis on the BPNNs as a function of the number of hidden layer and neurons.

sub-networks were tested using the untaught k_La values by Inga [58] and Martinez [66], as their studies were conducted with different gas–liquid systems, reactors geometries and operating conditions. Fig. 5 shows that the prediction of these untaught k_La values using the dimensional BPNN is acceptable with R^2 of 86% and standard deviation of 41%, whereas those for the dimensionless BPNN are 87 and 61%, respectively. This large standard deviation for the dimensionless BPNN could be related to the over-training of this BPNN and/or the inability of dimensionless numbers in providing accurate influence of all variables involved.

3.3. Predictions of k_La values using BPNNs

Fig. 6a and b shows that the dimensional and dimensionless BPNNs can predict k_La values with R^2 of 90.5 and 88.6%, and corresponding standard deviations of 23.3 and 24.1%, respectively. Figs. 7 and 8 compare the experimental k_La values with the predictions of the dimensionless correlations proposed by Wu [7] and Tekie et al. [8] in the SAR, and Chang [21] and Forrester et al. [24] in the GIR. From Figs. 6–8, it appears that the BPNN correlations provide good predictions, whereas the correlations by Wu [7], Tekie et al. [8], Chang [21] and Forrester et al. [24] fail to satisfactorily predict the majority of the experimental k_La values used in this study. This was expected since their correlations did not consider several important parameters, such as gas density, liquid surface tension or reactor geometry, whose influences on k_La are obviously significant.

Since acceptable agreements in both the validation and prediction steps were obtained with the dimensional BPNN, 3-dimensional response surfaces were generated and used to study the effect of liquid physicochemical

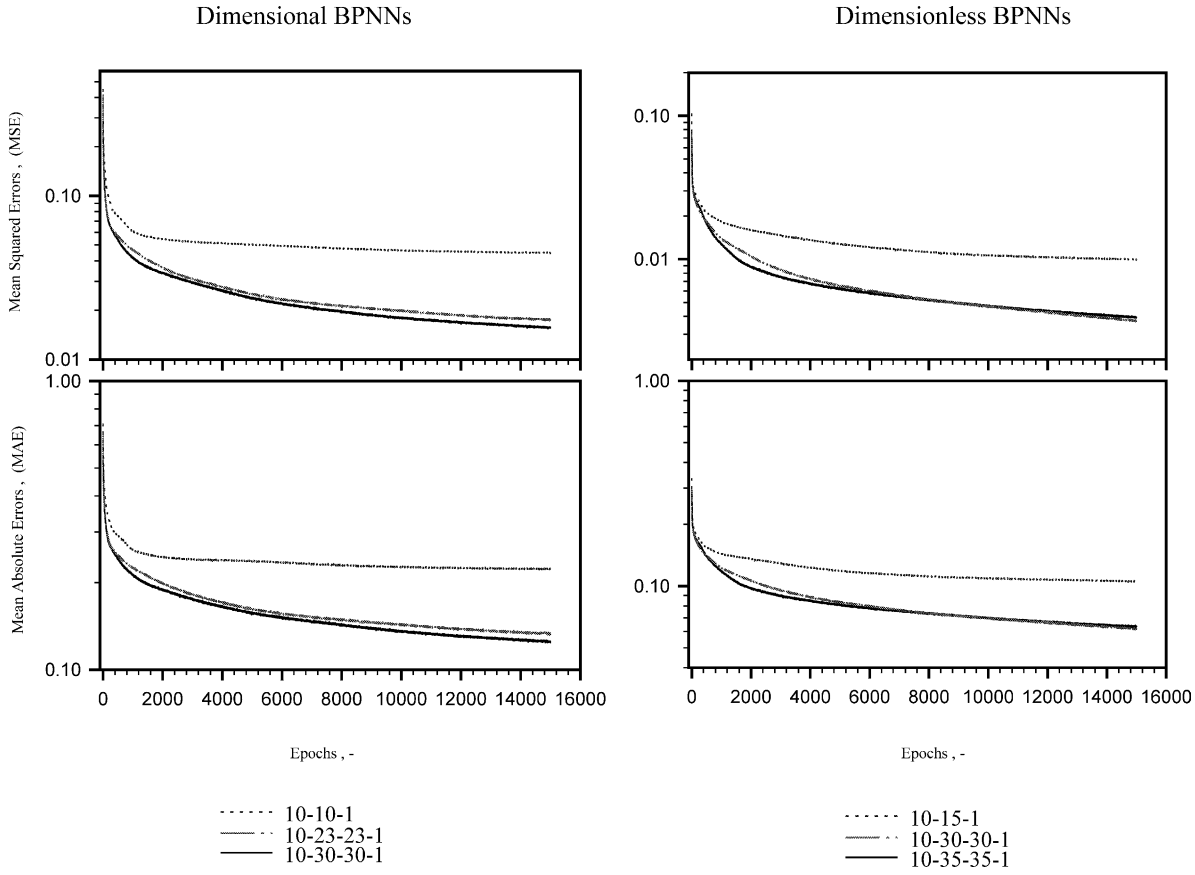

Fig. 4. Error analysis on the BPNNs as function of the epochs.

Table 7
Weights and biases of the 10-10-1 dimensional BPNN

Input weights $u_{i,j}$	1	2	3	4	5	6	7	8	9	10
1	−0.08	−6.61	−1.49	4.08	12.54	1.73	1.92	−1.11	−0.73	−2.53
2	−0.52	−4.06	4.71	3.25	−2.48	3.29	1.15	−4.42	−1.55	−11.52
3	1.85	0.15	−2.55	−1.17	−5.97	−3.59	−2.24	−2.30	−2.71	19.13
4	−2.08	2.18	0.32	1.21	5.10	−0.60	5.66	−1.43	−3.36	−6.35
5	−7.20	2.64	−2.68	−3.30	−4.08	−2.03	7.08	2.07	−4.01	−6.47
6	−0.32	−1.65	4.17	1.96	−1.42	3.29	−3.78	−1.56	−0.04	−6.71
7	3.09	1.30	−1.82	0.22	−3.25	−4.97	3.43	3.73	−2.91	−2.99
8	−8.38	−2.03	1.38	8.31	1.71	6.65	3.20	1.61	3.12	−2.02
9	−1.62	3.07	−0.16	−4.12	−0.96	4.03	2.35	−0.76	0.52	−1.82
10	10.79	8.01	−6.39	−2.87	3.00	−11.58	0.43	12.21	−7.31	−0.43
	1	2	3	4	5	6	7	8	9	10
Bias of hidden layer $u_{0,i}$	2.90	0.38	4.68	−0.88	6.59	−1.92	−2.53	0.34	1.20	−8.69
	1	2	3	4	5	6	7	8	9	10
Output weights w_i	1.68	2.83	−2.15	−2.84	−2.97	−4.25	4.30	1.50	4.67	−2.77
Bias of output neuron w_0					−2.33					

Table 8
Weights and biases of the 10-15-1 dimensionless BPNN

	1	2	3	4	5	6	7	8	9	10					
Input weights $u_{i,j}$															
1	−1.29	−5.11	−1.74	2.19	−12.71	−15.95	2.98	0.57	−0.83	3.47					
2	−0.29	2.69	−1.01	2.99	1.26	−1.71	−6.94	1.22	1.99	−2.06					
3	0.20	−3.89	−2.85	2.51	2.96	−12.51	7.72	−7.65	−9.90	−12.47					
4	4.37	−1.36	3.70	−3.22	−2.52	10.15	−0.21	−1.38	−0.62	−3.68					
5	0.53	−7.92	11.89	−0.68	2.09	6.66	0.68	−4.37	−5.37	2.86					
6	8.33	−6.88	7.03	−2.58	0.23	1.75	−13.77	3.82	−6.78	1.68					
7	−5.32	2.37	2.19	−8.26	1.92	−10.53	4.00	−4.57	0.27	2.46					
8	−2.52	8.02	−5.07	3.64	3.78	−13.32	6.07	−1.80	−1.74	1.33					
9	−0.30	4.93	−3.69	6.99	−10.05	6.77	−5.12	−0.21	2.72	0.49					
10	3.32	0.07	−4.60	−3.24	−11.54	−2.98	1.17	3.45	−1.86	2.91					
11	−1.62	3.20	−2.31	−24.67	−7.42	−3.71	0.29	0.51	−2.19	4.18					
12	2.15	−5.18	0.18	8.50	9.46	2.32	5.16	−4.96	−4.22	4.08					
13	4.12	9.82	−1.82	3.03	−9.84	11.56	−7.00	−1.66	−5.52	13.60					
14	0.86	−3.95	−9.76	−2.01	−3.74	−8.19	4.14	0.55	5.25	6.52					
15	0.52	−8.31	−1.38	3.06	0.15	−2.80	4.70	−8.07	−5.58	−10.76					
	1	2	3	4	5	6	7	8	9	10	11	12	13	14	15
Bias of hidden layer $u_{0,i}$	−1.19	−2.12	7.10	−3.90	−7.03	−4.17	1.72	−3.09	−2.90	0.52	−0.33	5.01	−1.29	−2.29	7.19
	1	2	3	4	5	6	7	8	9	10	11	12	13	14	15
Output weights w_i	−8.75	−2.16	5.52	−1.49	7.48	−1.55	−2.17	3.82	3.12	2.10	−5.52	1.62	−2.00	−0.79	−4.72
Bias of output neuron w_0							−0.36								

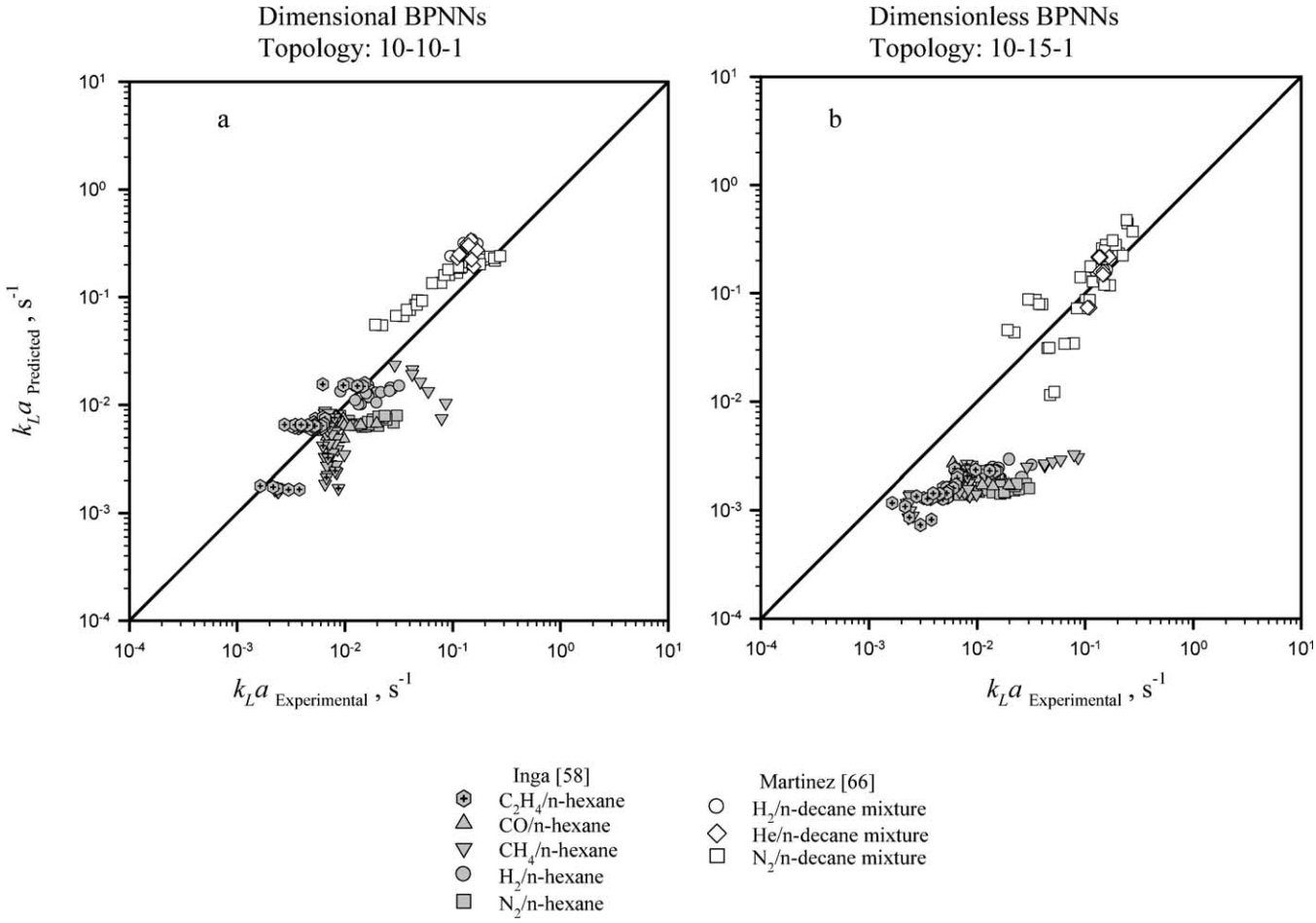

Fig. 5. Validation and interpolation of k_La values using the BPNNs.

properties, operating conditions and reactor geometries on k_La for different industrial processes as given in the following.

3.4. Effects of liquid physicochemical properties on k_La

Fig. 9a and b illustrates the effect of liquid viscosity on k_La, in the SAR and GIR, respectively. This is similar to the increase of liquid viscosity due to chemical reactions as in Fischer–Tropsch synthesis or hydrogenation of vegetable oil processes. As it can be observed in Fig. 9a, k_La decreases slightly with increasing liquid viscosity in the SAR, which is in agreement with literature data [3,4]. In the SAR, the gas–liquid interfacial area can be considered almost constant and accordingly the decrease of k_La with increasing viscosity can be attributed to the decrease of the mass transfer coefficient, k_L. In fact, an increase of the viscosity has been reported to decrease the turbulences at the gas–liquid surface leading to a decrease of the surface renewal rate and consequently k_L [10,55,67,68]. In the GIR, the gas–liquid interfacial area is not constant as gas bubbles are induced into the liquid when operating above the critical mixing speed for gas induction [69]. In a GSR, Rushton and Bimbinet [70] for water/corn syrup solution found that the gas holdup increases with liquid viscosity for μ_L values less than 5×10^{-3} Pa.s and then decreases with further increase in liquid viscosity. In a GIR, for water/CMC solution He et al. [71] reported similar findings which were attributed to the effect of liquid viscosity on the induced gas flow rate as described by Aldrich and van Deventer [72] and Fillion et al. [69]. Vermulen et al. [73] reported a rather slight decrease of the break-up rate, i.e. increase of the bubble coalescence with increasing liquid viscosity. Thus, if the effect of liquid viscosity on the gas holdup is stronger than that on the bubble size, the gas–liquid interfacial area, a is expected to increase and then decrease with increasing liquid viscosity. This means that increasing liquid viscosity could increase and decrease k_La due its resultant effect of a and k_L. In this study, the behavior of k_La follows that of k_L in the SAR, whereas in the GIR k_La is primarily affected by a rather than k_L, as can be seen in Fig. 9a and b, respectively.

Fig. 10a and b depicts the effect of liquid surface tension on k_La in the SAR and GIR. This figure could be used to speculate the effect of surface-active agents and impurities on k_La in biochemical processes. Fig. 10a

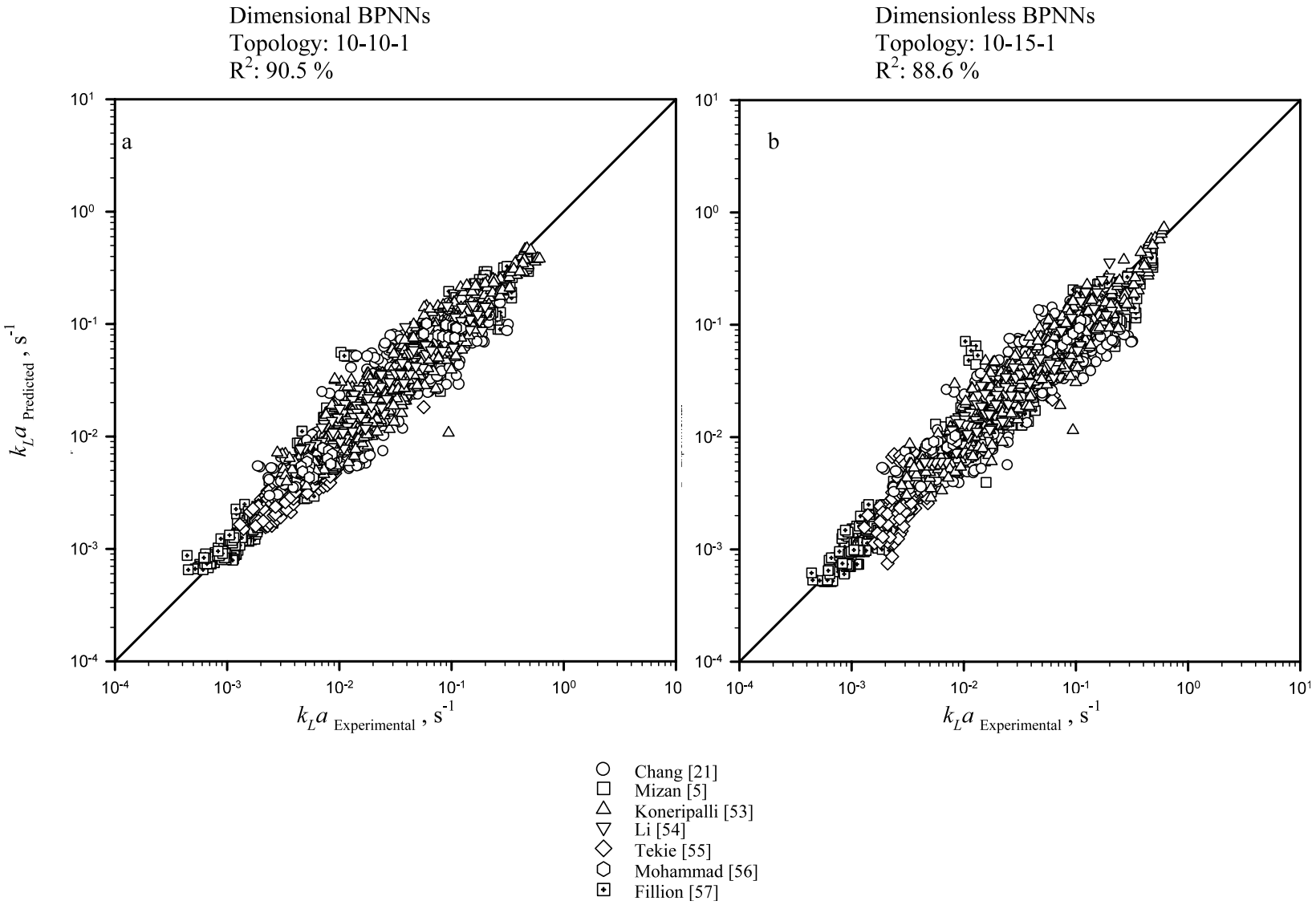

Fig. 6. Comparison between experimental and predicted $k_L a$ values of the BPNNs.

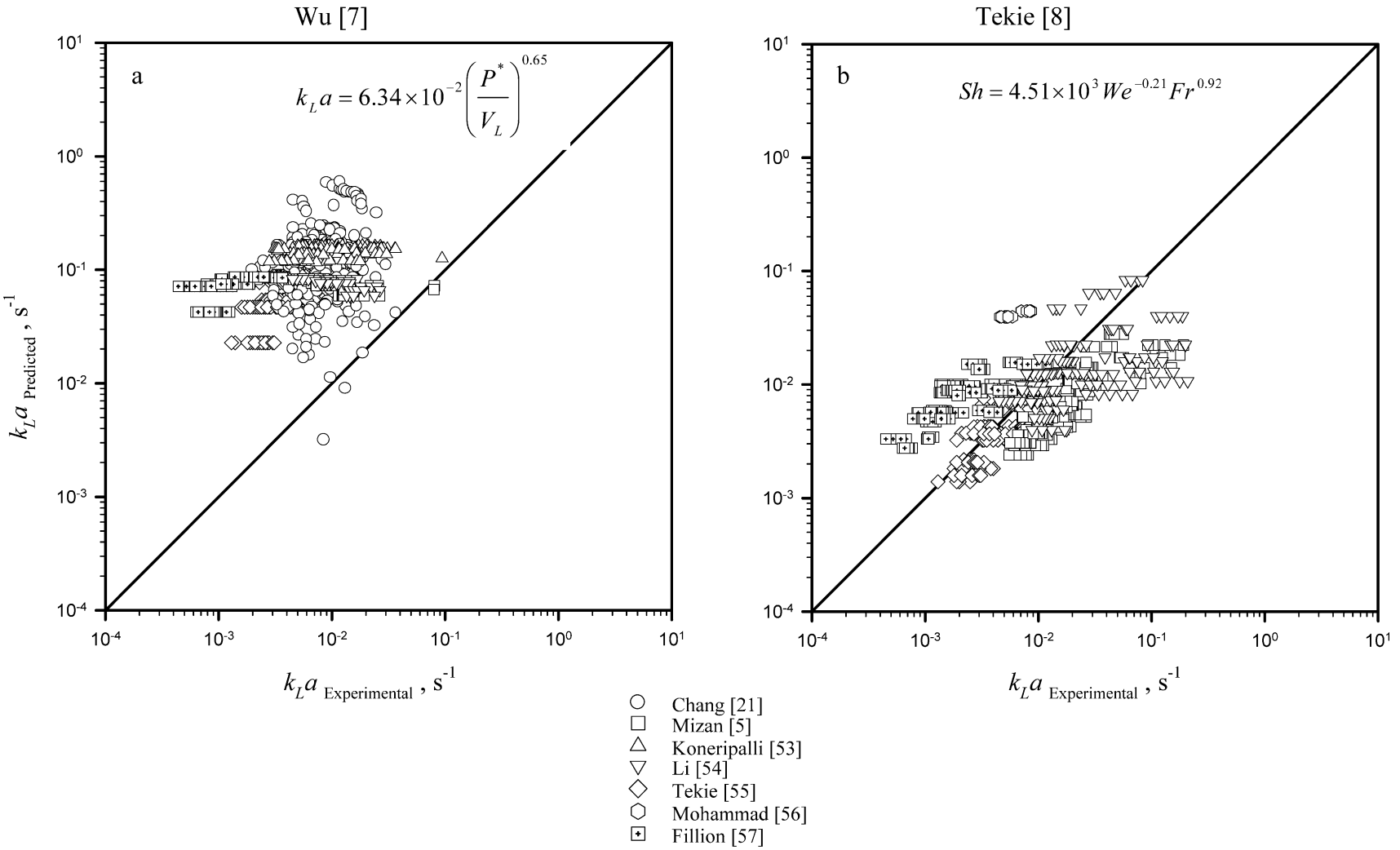

Fig. 7. Comparison between experimental and predicted $k_L a$ values from literature correlations in SAR.

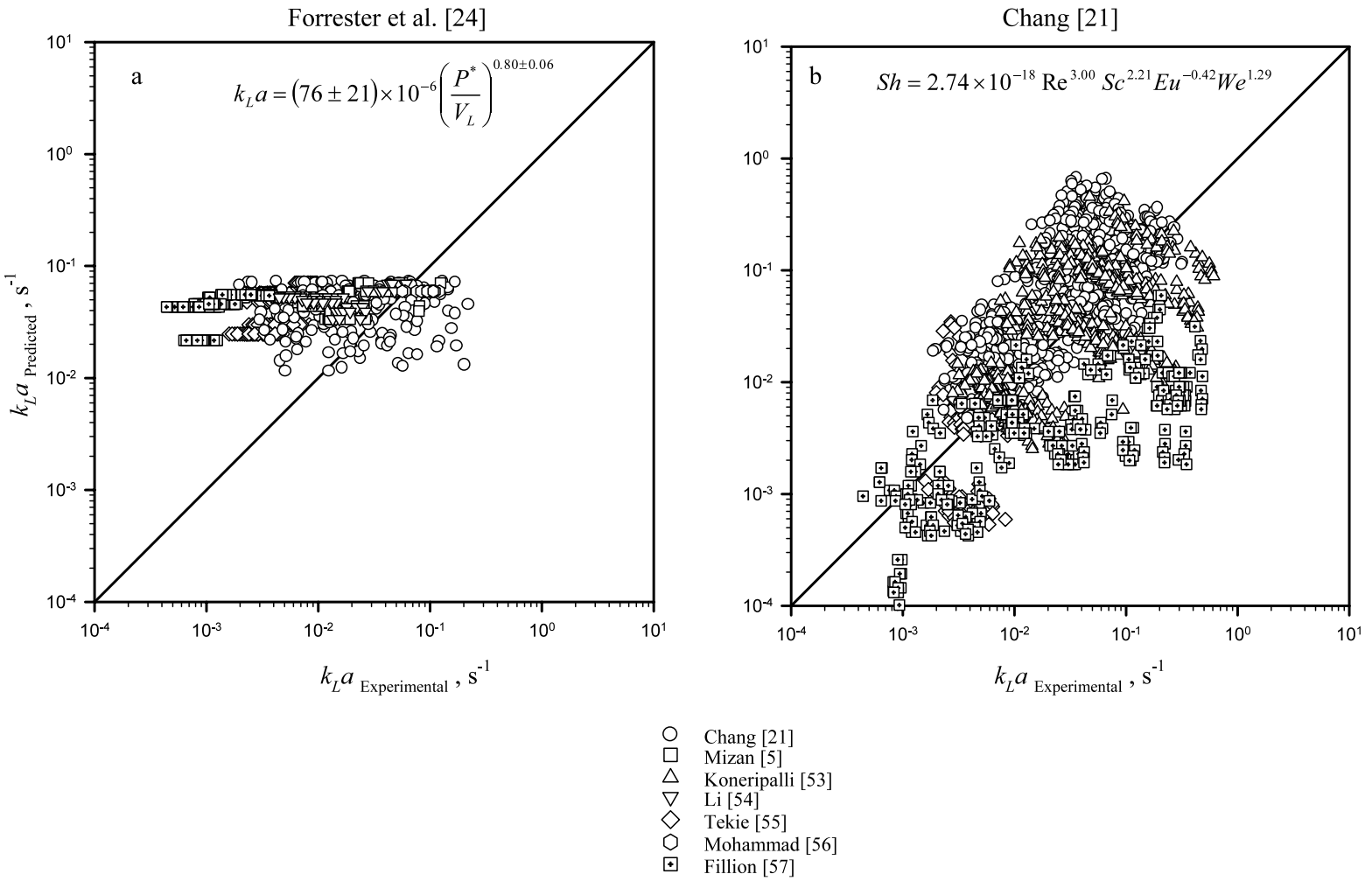

Fig. 8. Comparison between experimental and predicted $k_L a$ values from literature correlations in GIR.

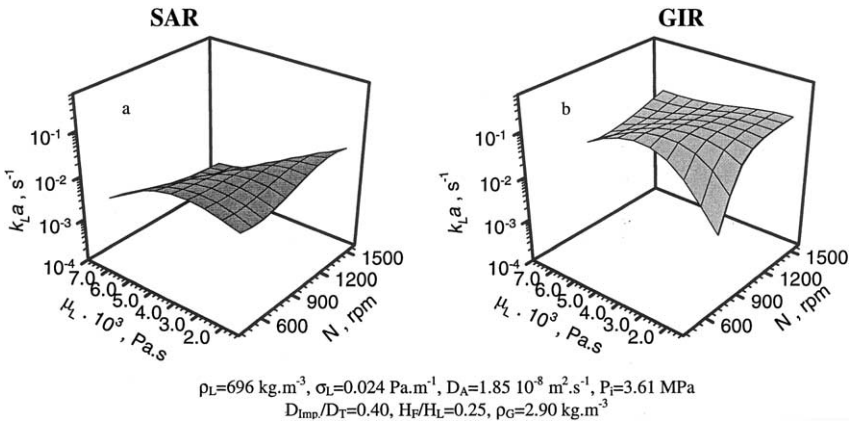

Fig. 9. Effect of viscosity and mixing speed on k_La values in SAR and GIR.

shows that k_La values obtained in the SAR increase with increasing liquid surface tension, which follows the behavior of k_L reported by Levich [74] and Davies [67], particularly under high turbulent conditions. In the GIR, k_La was found to slightly decrease with increasing liquid surface tension as illustrated in Fig. 10b. Calderbank [75] and Hinze [76] found that increasing liquid surface tension substantially increases the average bubble size in agitated reactors, which was found to decrease the gas holdup as reported by He et al. [71] and Albal et al. [3] in the GIR, and Calderbank [75] in the GSR. This means that although increasing liquid surface tension increases k_L, it decreases the gas–liquid interfacial area, which agrees with the findings by Patwardhan et al. [77] in the GIR and Calderbank [75] in the GSR. As a result of this behavior k_La could decrease or increase with increasing liquid surface tension in the GIR. In this study, the effect of liquid surface tension on a appears to be stronger than that on k_L leading to an increase of k_La with liquid surface tension in the GIR, as can be seen in Fig. 10b.

Fig. 11a and b shows the effect of liquid density on k_La in the SAR and GIR as an attempt to simulate the effect of changing liquid density during polymerization processes. As can be observed in this figure, k_La values seem to decrease with increasing liquid density in both reactor types. The available literature on the effect of liquid density on the mass transfer coefficient, however, is somewhat contradictory. For instance, Davies [67], Kosinski et al. [78] and Calderbank and Moo-Young [68] developed correlations where k_L is proportional to the liquid density to a power ranging from 1/4 to 1/2; however, Farritor and Hughmark [79], Boussinesq [80] and Higbie's penetration theory [81] reported no effect of liquid density on k_L. Furthermore, Zlokarnik [82], Aldrich and van Deventer [72] and Joshi and Sharma [11] studied the effect of liquid density on the induced gas flow rate in the GIR and concluded that an increase of liquid density resulted in an enhancement of the buoyancy forces acting on the gas bubbles which led to a decrease of the induced gas flow rate. This decrease of the induced gas flow rate with liquid density in the GIR decreases the gas holdup and subsequently the gas–liquid interfacial area. Therefore, it seems that k_La values decrease with increasing liquid density as a result of the decrease of the gas–liquid interfacial area in the GIR as illustrated in Fig. 11b. From the similarity of the k_La trends in both reactor types, however, it might be

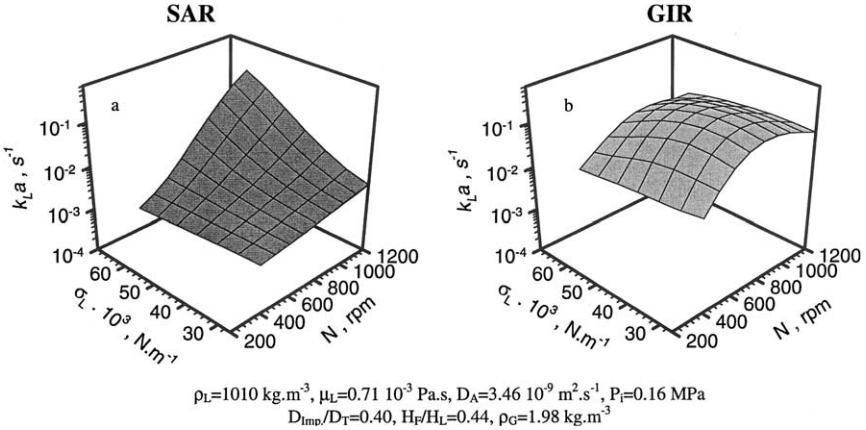

Fig. 10. Effect of surface tension and mixing speed on k_La values in SAR and GIR.

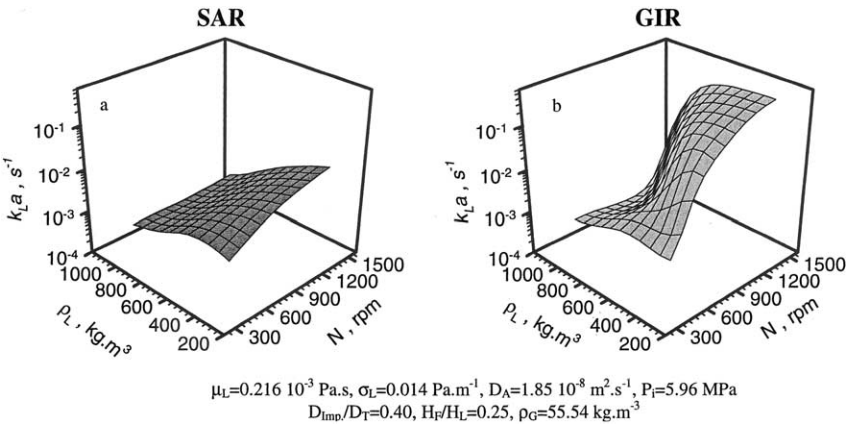

Fig. 11. Effect of liquid density and mixing speed on k_La values in SAR and GIR.

inferred that the decrease of k_La with increasing liquid density, observed in Fig. 11a, could be the result of decreasing bubble entrainment in the SAR, which was reported to occur by few investigators [2,3]. Nonetheless, it can be concluded that increasing liquid density decreases k_La as it affects primarily the gas–liquid interfacial area rather than k_L in both reactor types.

Fig. 12a and b shows the effect of diffusivity on k_La in the SAR and GIR which can be used to compare the effect of hydrogen and carbon dioxide diffusivities on k_La in Fischer–Tropsch synthesis. In both reactor types, k_La values were found to increase with increasing gas diffusivity, which is in accord with several literature findings [4,67,68,74,80,81,83]. For instance, Beenackers and van Swaaij [83] reported that k_L is proportional to the diffusivity to a power ranging from 0.5 for the penetration theory and 1.0 for the film model. Thus, it can be concluded that k_La increases with the diffusivity due to the increase of k_L, since the diffusivity is presumably independent of the gas–liquid interfacial area in both reactor types.

3.5. Effects of operating variables on k_La

Figs. 9–11a and b illustrate the effect of mixing speed on k_La in the SAR and GIR under operating conditions typical to different industrial processes. In agreement with the available literature on the SAR and GIR [2–13], k_La was found to increase with mixing speed. In the SAR, the interfacial area can be considered almost constant, and therefore the increase of k_La with N can essentially be attributed to the increase of k_L. Increasing N intensifies the turbulences and thus the surface renewal rate [10,55,79,83], which increases the mass transfer coefficient in the SAR. In the GIR, the gas–liquid interfacial area is not constant, since at the critical mixing speed for gas induction gas bubbles are induced into the liquid [69]. Above this critical mixing speed, further increase of N increases the induced gas flow rate [69,71,72], which increases the gas holdup [69,72] and the corresponding gas–liquid interfacial area [72]. Thus, both a and k_L and subsequently k_La values increase with mixing speed in the GIR. It should be mentioned,

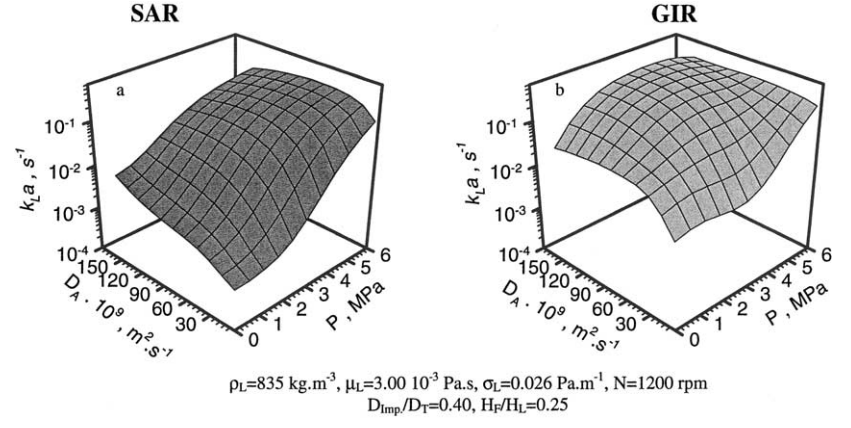

Fig. 12. Effect of diffusivity and gas partial pressure on k_La values in SAR and GIR.

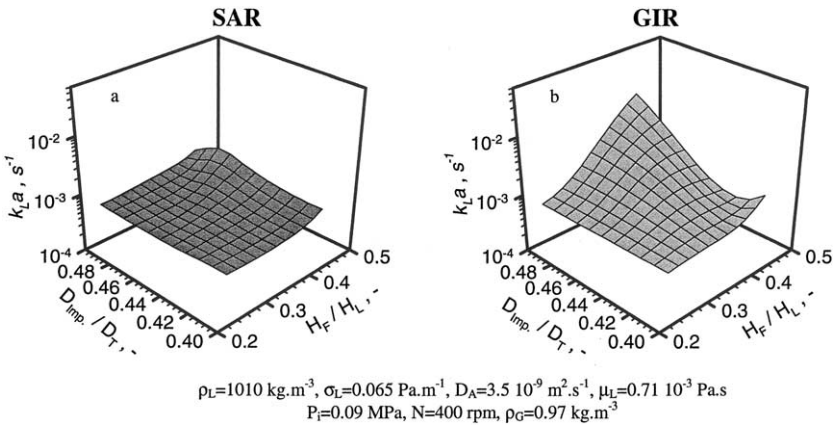

Fig. 13. Effect of reactor geometry on k_La values in SAR and GIR.

however, that k_La values start to level off at high mixing speeds (1200 rpm) indicating a fully developed hydrodynamic regime in the reactor [69].

Fig. 12a and b shows the effect of the gas partial pressure on k_La in the SAR and GIR, which could be used to simulate the change of CO and H_2 partial pressures due to chemical reactions in Fischer–Tropsch synthesis. The effect of pressure on k_La is rather contradictory as it was reported to be system-dependent in the literature [3–6,8–10,14–17,20–22,28,29,53–58,66,84–87]. In the SAR, however, the general trend is that k_L and subsequently k_La increase with pressure [3–6,8–10,20–22,28,29,53–58,66,84,85] due to the decrease of the system viscosity, which is similar to the behavior seen in Fig. 12a. In the GIR, literature data [88,89] indicated that an increase of pressure reduces the average bubble size, which results in an increase of the gas–liquid interfacial area, a [89]. Thus, in the GIR, both a and k_L increase with increasing gas partial pressure, leading to the increase of k_La as can be observed in Fig. 12b.

3.6. Effects of reactor geometry and operating mode on k_La

Fig. 13a and b presents the effect of $D_{Imp.}/D_T$ (impeller/reactor diameter ratio) and H_F/H_L (impeller height from the bottom of the reactor/liquid height ratio) on k_La for O_2 in water in the SAR and GIR, and as can be seen, k_La appears to increase with both ratios in the SAR, which is in agreement with the available literature [90–92]. It is generally accepted that an increase of $D_{Imp.}/D_T$ and H_F/H_L intensifies the turbulences at the gas–liquid surface, which leads to an increase of the surface renewal rate and thus k_L [74,79]. Under specific conditions, on the other hand, increasing both these ratios can result in an enhancement of surface entrainment in the SAR, which further increases the gas–liquid interfacial area [2,3]. Therefore, both a and k_L and subsequently k_La increase with increasing $D_{Imp.}/D_T$ and H_F/H_L in the SAR. In the GIR, similar results are observed as shown in Fig. 13b. In fact, an increase of $D_{Imp.}/D_T$ and H_F/H_L leads to an increase of the pumping capacity of the impeller, which results in an increase of the induced gas flow rate and subsequently the gas holdup [11,69,71]. This increase of gas holdup produces higher gas–liquid interfacial area, which in conjunction with an increase of k_L provides higher k_La values in the GIR.

Figs. 9–13a and b depict the effect of reactor operating mode on k_La for typical gases in a Fischer–Tropsch liquid, olefinic medium, vegetable oil and water. As can be observed in these figures, k_La values were found to be greater in the GIR than in the SAR. In fact, in the GIR above the critical mixing speed for gas induction [69], gas bubbles are induced in the liquid phase which creates additional gas–liquid interfacial area leading to higher k_La values than those in the SAR [10,55].

4. Conclusions

This study has demonstrated the potential of using ANNs as a correlation/prediction tool for k_La in SARs and GIRs. Using a large number of experimental data points (4435), one dimensional and one dimensionless BPNNs were constructed and successfully correlated k_La values of typical industrial processes under wide ranges of operating conditions. Due to its acceptable predictions, the dimensional BPNN was used to simulate and study the effect of physicochemical properties, operating conditions and reactor geometrical parameters on k_La in multiphase processes. The analysis of the predicted results led to the following conclusion:

1) Increasing liquid viscosity (such as in Fischer–Tropsch synthesis or hydrogenation of vegetable oil process due to chemical reaction) appeared to decrease k_La values in the SAR. In the GIR,

however, increasing liquid viscosity was found to increase and then decrease k_La values.

2) Increasing liquid density (such as in polymerization processes) resulted in a decrease of k_La values in both reactor types.
3) Increasing liquid surface tension (such as in biochemical processes) was found to decrease k_La in the GIR. In the SAR, however, increasing liquid surface tension appeared to increase k_La values.
4) Increasing gas diffusivity and partial pressure (such as in Fischer–Tropsch synthesis) resulted in an increase of k_La values in both reactor types.
5) k_La values appeared to increase with increasing mixing speed, and with $D_{Imp.}/D_T$ as well as H_F/H_L in the SAR and GIR for all the processes utilized in this study.
6) k_La values in the GIR appeared to be always higher than those in the SAR due to the increase of gas–liquid interfacial area in all the processes used in this study.

Even though the ANNs appeared to be a viable optimization and scale-up tool for industrial reactors, it should be mentioned that the use of a larger k_La database could further improve their predictive accuracy.

Appendix A: Nomenclature

a	interfacial area (m^{-1})
C_G	gas phase concentration ($kmol \cdot m^{-3}$)
C_L	liquid phase concentration ($kmol \cdot m^{-3}$)
D_A	diffusivity ($m^2 \cdot s^{-1}$)
$D_{Imp.}$	impeller diameter (m)
D_T	reactor diameter (m)
d_h	hydraulic diameter of Krischer–Kast $= d_P\sqrt[3]{16\varepsilon/9\pi(1-\varepsilon)^2}$ (m)
d_P	particle diameter (m)
d_V	sauter mean particle diameter (m)
E_0	activation energy (J)
H	liquid height above the impeller (m)
$H_{Imp.}$	impeller height (m)
H_B	baffles height (m)
H_L	liquid height (m)
H_F	height between the tank and impeller bottom (m)
h	heat transfer coefficient ($J.K^{-1} \cdot m^{-2} \cdot s^{-1}$)
k_L	mass transfer coefficient ($m \cdot s^{-1}$)
k_La	volumetric mass transfer coefficient (s^{-1})
N	mixing speed (rpm or Hz)
P_1	gas partial pressure (bar)
$P*$	power input (W)
R^2	regression coefficient (%)
T	temperature (K)
$u_{0,i}$	bias of the i^{th} hidden neuron (–)
$u_{i,j}$	weight between the i^{th} input neuron and the j^{th} hidden neuron (–)
u_{sb}	superficial bubble velocity ($m \cdot s^{-1}$)
U_G	superficial gas velocity ($m \cdot s^{-1}$)
U_L	superficial liquid velocity ($m \cdot s^{-1}$)
U_{Lmf}	minimum velocity of fluidization ($m \cdot s^{-1}$)
V_L	liquid volume (m^3)
w_0	bias of the output neuron (–)
w_i	weight between the i^{th} hidden neuron and the output neuron (–)
w_i	molar fraction of the compound i in the emulsion Tables 3 and 4 (–)
x_{10}	normalized input vector
x_1	coded variable for T (–)
x_2	coded variable for N (–)
x_3	coded variable for P (–)
x_4	coded variable for H (–)
y_{pred}	net input signal of the output neuron (–)
Y_{max}	maximum value of the trained output data set (–)
Y_{min}	minimum value of the trained output data set (–)
Y_{pred}	output signal of the output neuron (–)
y_i	molar fraction of the compound i in the bubbles Table 3 and Table 4 (–)
$z_{pred\ i}$	net input signal of the i^{th} hidden neuron (–)
$Z_{pred\ i}$	output signalof the i^{th} hidden neuron (–)

Greek letters

ε	porosity of the fixed bed (–)
ε_G	gas holdup (–)
μ	viscosity ($kg \cdot m^{-1} \cdot s^{-1}$ or $Pa \cdot s$)
ρ	density ($kg \cdot m^{-3}$)
σ	surface tension ($N \cdot m^{-1}$)

σ standard deviation: $\sigma = 100\times$

$$\sqrt{\frac{1}{N-1}\Sigma_{j=1}^{N}\left(\left|1-\frac{Y_{Pred,j}}{Y_{Exp,j}}\right|-\frac{100}{N}\Sigma_{i=1}^{N}\left|1-\frac{Y_{Pred,i}}{Y_{Exp,i}}\right|\right)^2} \quad (\%)$$

Abbreviations

ANN	artificial neural network
BPNN	back-propagation neural network
DNNC	dynamic neural network control
FF	feed forward
GIR	gas inducing reactor
GSR	gas sparging reactor
HLN	hidden layer neurons
ILN	input layer neurons
IU	international unit
MAE	mean absolute error
ML	multi-layer
MSE	mean squared error
OLN	output layer neurons
RMSE	root mean squared error
SAR	surface aeration reactor
SS conc	steady state concentration, (g/Nm^3 of H_2+CO)

Indices

L	liquid phase
G	gas phase
S	solid phase

Dimensionless numbers

Eu, Euler number	$P_1/(D_{Imp.}^2 \times \rho_L \times N^2)$
Fr, Froude number	$(D_{Imp.}^2 \times N^2)/g$
$Fr*$, modified Froude number	$N^2 D_{Imp}^2/g(H_L - H_F)$
Re, Reynolds number	$D_{Imp.}^2 \times \rho_L \times N^2/\mu_L$
Re_L, Reynolds number (bubble or particle)	$U_L \times \rho_L \times d_v/\mu_L$
Sc, Schmidt Number	$\mu_L/\rho_L \times D_A$
Sh, Sherwood number	$k_La \times D_{Imp.}^2/D_A$
Sh_G, Sherwood number (bubble or particle)	$k_La \times d_v^2/D_A$
$Sh*$, modified Sherwood number	$k_La/(g^2\rho_L/\mu_L)^{1/3}$
We, Weber number	$D_{imp.}^3 \times \rho_L \times N^2/\sigma_L$

Appendix B: Calculation procedure of the output signal

(1) The net input to (Z_1) is denoted (z_1) and is calculated as follow:

$$(z_1) = (u_0) + [\mathrm{u}](x_{10}) \tag{2}$$

The matrix [u] consists of n rows and 10 columns, corresponding to the number of input variables and nodes in the hidden layer 1:

$$[\mathrm{u}] = \begin{bmatrix} u_{1,1} & u_{1,2} & \cdots & u_{1,10} \\ u_{2,1} & \cdot & & \cdot \\ \cdot & & & \cdot \\ \cdot & & & \cdot \\ \cdot & & & \cdot \\ \cdot & & & \cdot \\ \cdot & & & \cdot \\ \cdot & & & \cdot \\ u_{n,1} & \cdots & & u_{n,10} \end{bmatrix} \tag{3}$$

It is also important to mention that each value of each input vector x_{10} was normalized as follows:

$$\text{Normalized value} = \frac{\text{Actual value} - \text{Minimum value of the data set}}{\text{Maximum value of the data set} - \text{Minimum value of the data set}} \tag{4}$$

(2) The activation function is applied to (z_1) to calculate the node output signal denoted (Z_1):

$$Z_1 = F(z_1) \tag{5}$$

(3) The net input to (Z_2) is denoted (z_2) and is calculated from the output signal, (Z_1):

$$z_2 = (v_0) + [\mathrm{v}](Z_1) \tag{6}$$

The matrix [v] consists of m rows and n columns, corresponding to the number of nodes in the hidden layer 2 and 1:

$$[\mathrm{v}] = \begin{bmatrix} v_{1,1} & v_{1,2} & \cdots & v_{1,n} \\ v_{2,1} & \cdot & & \cdot \\ \cdot & & & \cdot \\ \cdot & & & \cdot \\ \cdot & & & \cdot \\ \cdot & & & \cdot \\ \cdot & & & \cdot \\ \cdot & & & \cdot \\ v_{m,1} & \cdots & & v_{m,n} \end{bmatrix} \tag{7}$$

(4) As in 2, the activation function is applied to (z_2) to calculate the node output signal of the hidden layer 2, denoted (Z_2):

$$Z_2 = F(z_2) \tag{8}$$

(5) The net input to (Y_{pred}) is denoted (y_{pred}) and is calculated from the output signal, (Z_2) and the output weights, [w], as follow:

$$y_{\mathrm{pred}} = w_0 + [\mathrm{w}](Z_2) \tag{9}$$

In this study, the output matrix of the weights consists of 1 row and m columns

(6) Finally, the activation function is applied again to y_{pred} to calculate the output value, Y_{pred}:

$$Y_{\mathrm{pred}} = F(y_{\mathrm{pred}}) \tag{10}$$

In addition, since the PITTNET program normalizes all vectors, the outputs (target) for the dimensional and dimensionless BPNNs, $\ln(k_L a)$ and $\log(Sh)$ respectively, were calculated as follows:

$$\ln(k_L a) \text{ or } \log(Sh) = Y_{\mathrm{pred}} \times (Y_{\max} - Y_{\min}) + Y_{\min} \tag{11}$$

With $Y_{\max}$ and $Y_{\min}$ given in Table 6.

References

[1] P.L. Mills, R.V. Chaudhari, Reaction engineering of emerging oxidation processes, Catalysis Today 48 (1999) 17–29.

[2] M.H. Matsumura, H. Masunaga, J. Kobayashi, Gas absorption in an aerated stirred tank at high power input, J. Ferment. Technol. 57 (1979) 107–116.

[3] R.S. Albal, Y.T. Shah, A. Shumpe, N.L. Carr, Mass transfer in multiphase agitated reactor, Chem. Eng. J. 27 (1983) 67–80.

[4] G.F. Versteeg, P.M.M. Blauwhoff, W.P.M. van Swaaij, The effect of diffusivity on gas–liquid mass transfer in stirred vessels. Experiments at atmospheric and elevated pressures, Chem. Eng. Sci. 42 (1987) 1103–1119.

[5] T.I. Mizan, Characterization of mass transfer of gases in olefinic polymerization solvents and slurries in agitated reactors, MS. Dissertation, University of Pittsburgh, Pittsburgh, PA, USA, 1992.

[6] T.I. Mizan, J. Li, B.I. Morsi, M.-Y. Chang, E. Maier, C.P.P. Singh, Solubilities and mass transfer coefficients of gases in liquid propylene in a surface-aeration agitated reactor, Chem. Eng. Sci. 49 (1994) 821–830.

[7] H. Wu, An issue on applications of a disk turbine for gas–liquid mass transfer, Chem. Eng. Sci. 50 (1995) 2801–2811.

[8] Z. Tekie, J. Li, B.I. Morsi, M.-Y. Chang, Gas–liquid mass transfer in cyclohexane oxidation process using gas-inducing and surface-aeration agitated reactors, Chem. Eng. Sci. 52 (1997) 1541–1551.

[9] Z. Tekie, J. Li, B.I. Morsi, Mass transfer parameters of O_2 and N_2 in cyclohexane under elevated pressures and temperatures: a statistical approach, Ind. Eng. Chem. Res. 36 (1997) 3879–3888.

[10] B. Fillion, B.I. Morsi, Gas–liquid mass-transfer and hydrodynamic parameters in a soybean oil hydrogenation process under industrial conditions, Ind. Eng. Chem. Res. 39 (2001) 2157–2168.

[11] J.B. Joshi, M.M. Sharma, Mass transfer and hydrodynamic characteristics of gas-inducing type of agitated contactors, Can. J. Chem. Eng. 65 (1977) 683–695.

[12] Kara M. An Experimental Study of Hydrogen Mass Transfer Rate in Liquid Hydrocarbons at High Temperatures and Pressures, Ph.D. Dissertation, University of Pittsburgh, Pittsburgh, PA, USA, (1981).

[13] S.B. Sawant, J.B. Joshi, V.G. Pangarkar, R.D. Mhaskar, Mass transfer and hydrodynamic characteristics of the denver type of flotation cells, Chem. Eng. J. 21 (1981) 11–19.

[14] B.M. Karandikar, B.I. Morsi, Y.T. Shah, N.L. Carr, Effect of water on the solubilities and mass transfer coefficients of gases in a heavy fraction of Fischer-Tropsch products, Can. J. Chem. Eng. 65 (1987) 973–981.

[15] M.-Y. Chang, J.G. Eiras, B.I. Morsi, Mass transfer characteristics of gases in n-hexane at elevated pressures and temperatures in agitated reactors, Chem. Eng. Process. 29 (1991) 49–60.
[16] M.-Y. Chang, B.I. Morsi, Mass transfer characteristics of gases in aqueous and organic liquids at elevated pressures and temperatures in agitated reactors, Chem. Eng. Sci. 46 (1991) 2639–2650.
[17] M.-Y. Chang, B.I. Morsi, Mass transfer characteristics of gases in n-decane at elevated pressures and temperatures in agitated reactors, Chem. Eng. J. 47 (1991) 33–45.
[18] E. Dietrich, C. Mathieu, H. Delmas, J. Jenck, Raney-Nickel catalyzed hydrogenations: gas–liquid mass transfer in gas-induced stirred slurry reactors, Chem. Eng. Sci. 47 (1992) 3597–3604.
[19] H. Hichri, A. Accary, J. Andrieu, Kinetics and slurry-type reactor modeling during catalytic hydrogenation of *o*-cresol on Ni/SiO_2, Chem. Eng. Process. 30 (1991) 133–140.
[20] M.-Y. Chang, B.I. Morsi, Solubilities and mass transfer coefficients of carbon monoxide in a gas-inducing reactor operating with organic liquids under high pressures and temperatures, Chem. Eng. Sci. 47 (1992) 3541–3548.
[21] Chang M.-Y., Mass Transfer Characteristics of Gases in Aqueous and Organic Liquids at Elevated Pressures and Temperatures in Agitated Reactors, Ph.D. Dissertation, University of Pittsburgh, Pittsburgh, PA, USA, (1991).
[22] N. Koneripalli, Z. Tekie, B.I. Morsi, Mass transfer characteristics of gases in methanol and ethanol under elevated pressures and temperatures, Chem. Eng. J. 54 (1994) 63–77.
[23] A. Heim, A. Kraslawski, E. Rzyski, J. Stelmach, Aeration of bioreactors by self-aspirating impellers, Chem. Eng. J. 58 (1995) 59–63.
[24] S.E. Forrester, C.D. Rielly, K.J. Carpenter, Gas-inducing impeller design and performance characteristics, Chem. Eng. Sci. 53 (1998) 603–615.
[25] H. Yang, B.S. Fang, M. Reuss, k_La correlation established on the basis of a neural network model, Can. J. Chem. Eng. 77 (1999) 838–843.
[26] J. Reisener, M.A. Reuter, J. Krüger, Modeling of the mass transfer in gas-sparged electrolysers with neural networks, Chem. Eng. Sci. 48 (1993) 1089–1101.
[27] F. García-Ochoa, E. Gómez Castro, Estimation of oxygen mass transfer coefficient in stirred tank reactors using artificial neural networks, Enz. Micro. Tech. 28 (2001) 560–569.
[28] J. Li, Z. Tekie, A. Mohammad, B.I. Morsi, Statistical assessment of gas/liquid mass transfer in slurry-phase propylene polymerization process, Can. J. Chem. Eng. 74 (1996) 77–83.
[29] J.R. Inga, B.I. Morsi, Effect of catalyst loading on gas/liquid mass transfer in slurry reactors: a statistical experimental approach, Can. J. Chem. Eng. 75 (1997) 872–881.
[30] E. Alvarez, J.M. Correa, C. Riverol, J.M. Navaza, Model based in neural networks for the prediction of the mass transfer coefficients in bubble columns. study in Newtonian and non-Newtonian fluids, Int. Comm. Heat Mass Transfer 27 (2000) 93–98.
[31] M.A. Hussain, Review of the applications of neural networks in chemical process control–simulation and online implementation, Art. Intel. Eng. 13 (1999) 55–68.
[32] M. Fullana, F. Trabelsi, F. Recasens, Use of neural net computing for statistical and kinetic modeling and simulation of supercritical fluid extractors, Chem. Eng. Sci. 55 (2000) 79–95.
[33] H.M. Henrique, E.L. Lima, D.E. Seborg, Model structure determination in neural network models, Chem. Eng. Sci. 55 (2000) 5457–5469.
[34] Y.P. I, W.T. Wu, Y.C. Liu, Neural network modeling for on-line state estimation in fed-batch culture of L-lysine production, Bio. Eng. J. 61 (1996) 35–40.
[35] I. Iliuta, F. Larachi, B.P.A. Grandjean, G. Wild, Gas–liquid interfacial mass transfer in trickle-bed reactors: state of the art correlations, Chem. Eng. Sci. 54 (1999) 5633–5645.
[36] K. Jambunathan, S.L. Hartle, S. Ashforth-Frost, V.N. Fontama, Evaluating convective heat transfer coefficients using neural networks, Int. J. Heat Mass Transfer 39 (1996) 2329–2332.
[37] M. Krothapally, S. Palanki, A neural network strategy for batch process optimization, Comp. Chem. Eng. 21 (1997) 463–468.
[38] F. Larachi, I. Iliuta, O. Rival, B.P.A. Grandjean, Prediction of minimum fluidization velocity in three-phase fluidized-bed reactors, Ind. Eng. Chem. Res. 39 (2000) 563–572.
[39] T.M. Leib, P.L. Mills, J.J. Lerou, Fast response distributed parameters fluidized bed reactor model for propylene partial oxidation using feed-forward neural network methods, Chem. Eng. Sci. 51 (1996) 2189–2198.
[40] T.M. Leib, P.L. Mills, J.J. Lerou, J.R. Turner, Evaluation of neural networks for simulation of three-phase bubble column reactors, Trans IchemE 73 (Part A) (1995) 690–696.
[41] P.M. Mills, A.Y. Zomaya, M.O. Tade, Adaptive model-based control using neural networks, Int. J. Control 60 (1994) 1163–1192.
[42] C.A.O. Nascimento, R. Giudici, Neural network based approach for optimization applied to an industrial nylon-6,6 polymerization process, Comp. Chem. Eng. 22 (1998) 595–600.
[43] C.A.O. Nascimento, R. Giudici, R. Guardani, Neural network based approach for optimization of industrial chemical processes, Comp. Chem. Eng. 24 (2000) 2303–2314.
[44] NikraveshM., T.G. Farrell, Stanford, Control of nonisothermal CSTR with time varying parameters via dynamic neural network control (DNNC), Chem. Eng. J. 76 (2000) 1–16.
[45] H. Qi, X.G. Zhou, L.H. Liu, W.K. Yuan, A hybrid neural network-first principles model for fixed-bed reactor, Chem. Eng. Sci. 54 (1999) 2521–2526.
[46] B.K. Sharma, M.P. Sharma, S.K. Roy, S. Kumar, S.B. Tendulkar, S.S. Tambe, B.D. Kulkarni, Fischer-Tropsch synthesis with Co/SiO_2-Al_2O_3 catalyst and steady-state modeling using artificial neural networks, Fuel 77 (1998) 1763–1768.
[47] A.M. Shaw, F.J. Doyle, III, J.S. Schwaber, A dynamic neural network approach to nonlinear process modeling, Comp. Chem. Eng. 21 (1996) 371–385.
[48] S.B. Tendulkar, S.S. Tambe, I. Chandra, P.V. Rao, R.V. Naik, B.D. Kulkarni, Hydroxylation of phenol to dihydroxybenzenes: development of artificial neural-network-based process identification and model predictive control strategies for a pilot plant scale reactor, Ind. Eng. Chem. Res. 37 (1998) 2081–2085.
[49] J. Thibault, B.P.A. Grandjean, A neural network methodology for heat transfer data analysis, J. Heat Mass Transfer 34 (1991) 2063–2070.
[50] J.A. Wilson, F.M. Zorzetto, A generalized approach to process state estimation using hybrid artificial neural network/mechanistic models, Comp. Chem. Eng. 21 (1996) 951–963.
[51] X.G. Zhou, L.H. Liu, Y.C. Dai, W.K. Yuan, Modeling of a fixed-bed reactor using the K-L expansion and neural networks, Chem. Eng. Sci. 51 (1996) 2179–2188.
[52] L. Fausset, Fundamentals of Neural Networks: Architectures, Algorithms and Applications, Prentice Hall inc, Englewood Cliffs, New Jersey, 1994.
[53] Koneripalli N., Mass Transfer Characteristics of Gases in Methanol and Ethanol Under Elevated Pressures and Temperatures in Agitated Reactors, Ph.D. Dissertation, University of Pittsburgh, Pittsburgh, PA, USA, (1992).
[54] Li J., Mass Transfer and Mathematical Modeling For Propylene Polymerization Process, Ph.D. Dissertation, University of Pittsburgh, Pittsburgh, PA, USA, (1995).
[55] Tekie Z., Mass Transfer and Modeling of Liquid-Phase Cyclohexane Oxidation Process in Agitated Reactors, Ph.D. Dissertation, University of Pittsburgh, Pittsburgh, PA, USA, (1997).

[56] Mohammad A., Gas–Liquid Mass Transfer Parameters in Benzoic Acid Oxidation Process, Ph.D. Dissertation, University of Pittsburgh, Pittsburgh, PA, USA, (1999).
[57] Fillion B., Modeling of Soybean Oil Hydrogenation Process, Ph.D. Dissertation, University of Pittsburgh, Pittsburgh, PA, USA, (2001).
[58] Inga J.R., Scale-up and Scale-down of Slurry Reactors: A New Methodology, Ph.D. Dissertation, University of Pittsburgh, Pittsburgh, PA, USA, (1997).
[59] J.C. Charpentier, Mass Transfer Rates in Gas–Liquid Absorbers and Reactors, Advances in Chemical Engineering, Academic Press, 1981, p. 11.
[60] E. Buckingham, On physical similar systems: illustrations of the use of dimensional equations, Phys. Rev. 4 (1914) 345–376.
[61] Rumelhart D.E., G.E. Hinton and R.J. Williams, Learning Internal Representations by Error Propagation, Parallel Distributed Processing: Explorations in the Microstructure of Cognition, MA: The MIT Press, Foundations D.E. Rumelhart and J.L. McClelland (eds.), Vol. 1 (1986), pp. 318-362.
[62] K. Funahashi, On the approximate realization of continuous mappings by neural networks, Neural Networks 2 (1989) 183–192.
[63] K. Hornik, M. Stinchcombe, H. White, Multilayer feedforward networks are universal approximators, Neural Networks 2 (1989) 359–366.
[64] S. German, E. Bienenstock, R. Doursat, Neural networks and the bias/variance dilemma, Neural Comput. 4 (1992) 1–58.
[65] J.M. Twomey, A.E. Smith, Bias and variance of vadidation methods for function approximation neural networks under conditions of sparse data, IEEE Trans. Syst. Man Cybern. 28 (3 Part C) (1998) 417–430.
[66] Martinez B. Mass Transfer Parameters of H_2 and N_2 in a Slurry Agitated Reactor Operating under Industrial Conditions with Organic Liquid Mixtures, M.S. Dissertation, University of Pittsburgh, Pittsburgh, PA, USA (2000).
[67] J.T. Davies, Turbulence phenomena at free surfaces, AIChE J. 18 (1972) 169–173.
[68] P.H. Calderbank, M.B. Moo-Young, The continuous phase heat and mass-transfer properties of dispersion, Chem. Eng. Sci. 16 (1961) 39–54.
[69] Fillion B., R. Lemoine, Y. Heintz and B.I. Morsi, Characterization of Gas-Inducing Impeller at Elevated Temperatures and Pressures, in press.
[70] J.H. Rushton, J.-J. Bimbinet, Holdup and flooding in air liquid mixing, Canad. J. Chem. Eng. 46 (1968) 16–21.
[71] D.X. He, S.H. Chiang, G.E. Klinzing, Operating characteristics of a gas/liquid contactor using gas-inducing turbine, J. Chin. Inst. Chem. Eng. 22 (1991) 321–328.
[72] C. Aldrich, J.S.J. van Deventer, Observations on the effect of medium density and viscosity on the rate of induced aeration in agitated vessels, Metal. Mat. Trans. B. 25B (1994) 303–306.
[73] T. Vermulen, G.M. Williams, G.E. Langlois, Chem. Eng. Prog. 51 (1955) 2(85F).
[74] V.G. Levich, Physicochemical Hydrodynamics, Prentice-Hall, Englewood Cliffs NJ, 1962, pp. 689–697.
[75] P.H. Calderbank, Physical rate processes in industrial fermentation. part I: the interfacial area in gas–liquid contacting with mechanical agitation, Trans. Inst. Chem. Eng. 36 (1958) 443–463.
[76] J.O. Hinze, Fundamentals of the hydrodynamic mechanism of splitting in dispersion processes, AIChE J. 1 (1955) 289.
[77] A.W. Patwardhan, J.B. Joshi, Design of gas-inducing reactors, Ind. Eng. Chem. Res. 38 (1999) 49–80.
[78] A.A. Kosinski, C.J. King, The influence of diffusivity on liquid phase mass transfer to the free interface in a stirred vessel, AIChE J. 12 (1966) 109–116.
[79] R.E. Farritor, G.A. Hughmark, Mass transfer to the free interface in a stirred vessel, AIChE J. 20 (1974) 1027–1028.
[80] J. Boussinesq, J. Math. 6 (1905) 285.
[81] R. Higbie, The rate of absorption of a pure gas into a still liquid during short periods of exposure, Trans. Am. Inst. Chem. Eng. 31 (1935) 365.
[82] M. Zlokarnik, Hollow stirrers for gassing of liquids. Determination of gas diffusion and wave performance, Chem. Ing. Eng. 38 (1966) 357–366.
[83] A.A.C.M. Beenackers, W.P.M. van Swaaij, Mass transfer in gas–liquid slurry reactors, Chem. Eng. Sci. 48 (1993) 3109–3139.
[84] A. Deimling, B.M. Karandikar, Y.T. Shah, N.L. Carr, Solubility and mass transfer of CO and H_2 in Fischer-Tropsch liquids and slurries, Chem. Eng. J. 29 (1984) 127–140.
[85] J.H. Lee, N.R. Foster, Mass transfer and solubility of O_2 and CH_4 in silicone fluids, Ind. Eng. Chem. Res. 29 (1990) 691–696.
[86] F. Yoshida, S.-I. Arakawa, Pressure dependency of liquid phase mass transfer coefficients, AIChE J. 14 (1968) 962–963.
[87] M. Teramoto, S. Tai, K. Nishii, H. Teranishi, Effects of pressure on liquid-phase mass transfer coefficients, Chem. Eng. J. 8 (1974) 223–226.
[88] M.P. Wilkinson, H. Haringa, L.L. van Dierendonck, Mass transfer and bubble size in a bubble column under pressure, Chem. Eng. Sci. 49 (1994) 1417–1427.
[89] T. Sridhar, O.E. Potter, Gas holdup and bubble diameter in pressurized gas–liquid stirred vessels, Ind. Eng. Chem. Fundam. 19 (1980) 21–26.
[90] V.D. Metha, M.M. Sharma, Mass transfer in mechanically agitated gas–liquid contactors, Chem. Eng. Sci. 26 (1971) 461.
[91] H. Judat, Gas/liquid mass transfer in stirred vessels-a critical review, Ger. Chem. Eng. 5 (1982) 357.
[92] R.V. Chaudhari, R.V. Gholap, G. Emig, H. Hofmann, Gas–liquid mass transfer in dead-end autoclave reactors, Can. J. Chem. Eng. 65 (1987) 774.